Diffusion of the Second Messengers in the Cytoplasm Acts as a Variability Suppressor of the Single Photon Response in Vertebrate Phototransduction

Paolo Bisegna,* Giovanni Caruso,† Daniele Andreucci,‡ Lixin Shen,§¶ Vsevolod V. Gurevich,§ Heidi E. Hamm,§¶ and Emmanuele DiBenedetto¶‖

*Department of Civil Engineering, University of Rome, Tor Vergata, Italy; †Construction Technologies Institute, National Research Council, Rome, Italy; ‡Department of Mathematical Methods and Models, University of Rome, La Sapienza, Italy; and §Department of Pharmacology, Vanderbilt University Medical Center, ¶Biomathematics Study Group, Vanderbilt University Medical Center, ‖Department of Mathematics, Vanderbilt University, Nashville, Tennessee

ABSTRACT The single photon response in vertebrate phototransduction is highly reproducible despite a number of random components of the activation cascade, including the random activation site, the random walk of an activated receptor, and its quenching in a random number of steps. Here we use a previously generated and tested spatiotemporal mathematical and computational model to identify possible mechanisms of variability reduction. The model permits one to separate the process into modules, and to analyze their impact separately. We show that the activation cascade is responsible for generation of variability, whereas diffusion of the second messengers is responsible for its suppression. Randomness of the activation site contributes at early times to the coefficient of variation of the photoresponse, whereas the Brownian path of a photoisomerized rhodopsin (Rh*) has a negligible effect. The major driver of variability is the turnoff mechanism of Rh*, which occurs essentially within the first 2–4 phosphorylated states of Rh*. Theoretically increasing the number of steps to quenching does not significantly decrease the corresponding coefficient of variation of the effector, in agreement with the biochemical limitations on the phosphorylated states of the receptor. Diffusion of the second messengers in the cytosol acts as a suppressor of the variability generated by the activation cascade. Calcium feedback has a negligible regulatory effect on the photocurrent variability. A comparative variability analysis has been conducted for the phototransduction in mouse and salamander, including a study of the effects of their anatomical differences such as incisures and photoreceptors geometry on variability generation and suppression.

INTRODUCTION

Vertebrate rod photoreceptors are capable of detecting the absorption of a single photon with a wavelength of ~500 nm (1,2). Moreover, the resulting responses are highly reproducible, in the sense that the peak amplitudes and the shapes of the photocurrent as a function of time are very similar. Quantitatively, repeated single photon activations yield peak photocurrents with coefficient of variation (CV), defined as the ratio of the standard deviation to the mean, of ~20% (3,4). It is generally believed that a key contributor to this high fidelity of the single photon response (SPR) is the amplification part of the cascade (5–12).

One of the main points of this article is to challenge this assumption. We demonstrate that the diffusion of the second messengers cyclic guanosine-monophosphate (cGMP) and Ca^{2+} in the rod cytoplasm with characteristic complex geometry (13–15), after the activation of the photocascade, is the key determinant of the high reproducibility of the response.

The experimental results of the literature (6–8) have a photon as input and the photocurrent as output, and variability of the resulting photocurrent is statistically estimated. We show that the variation of the photocurrent is determined by two distinct modules, the activation cascade and the diffusion of cGMP and Ca^{2+}, each contributing differently to the reproducibility of the response. Our modeling shows that the activation cascade and the random shutoff mechanism of a photoisomerized rhodopsin (Rh*) yields a CV of the total number of activated effectors, of ~60%, whereas the diffusion of the second messengers reduces it to the observed 40% for the integration time and to ~20% for the photocurrent at peak time. These two components, which cannot be distinguished using existing experimental techniques, can be mathematically separated into two modules and analyzed separately.

We show that the random walk of the Rh* after photoactivation, and the randomness of the activation site, contribute negligibly to the CV of the response. The main contributor to the variability seems to be the random shutoff mechanism of Rh*.

Finally, an experimentally observed CV of ~20% for the current amplitude at peak time is obtained with Rh* shutting off through 2–3, at most, phosphorylated states. This is determined by numerical modeling and simulations of the CV as a function of the underlying biochemistry.

Molecules of receptor rhodopsin (Rh), transducin G-protein (T), and effector phosphodiesterase (E), are regarded as freely diffusing particles on the two-dimensional disk sur-

Submitted June 4, 2007, and accepted for publication November 21, 2007.

Address reprint requests to Emmanuele DiBenedetto, E-mail: em.diben@vanderbilt.edu.

Editor: Jennifer Linderman.

© 2008 by the Biophysical Society

0006-3495/08/05/3363/21 $2.00

doi: 10.1529/biophysj.107.114058

face, each with their own specific diffusivity. The original signal of a single photon-activating molecule of Rh is amplified in the sense that an Rh* activates along its random walk, during the time it remains active, dozens of transducins (T → T*), by catalyzing GDP/GTP exchange on their α-subunit. Each molecule of T* associates, one-to-one, with a catalytic subunit of the effector forming a T*·E complex, denoted by E*, and called the activated-effector. The full-activation hypothesis postulates that a molecule of PDE is active only if both its subunits are bound to a molecule of T*. Thus, assuming full activation, [PDE*] = 1/2[E*].

A single molecule of E*, during its lifetime, hydrolyzes in excess of 50 molecules of the second messenger, cGMP (16,17). Diffusion of cGMP away from the cationic channels that it keeps open causes channel closure, and thereby suppresses the inward current. Low variability (high fidelity) of the SPR is experimentally assessed in terms of this photocurrent (3,4,6–8).

The strength of the output signal depends on the number of activated effectors E*, which in turn depends on the active lifetime of Rh*, and their own active lifetime. Inactivation of Rh* occurs essentially by two molecular events. First Rh* is phosphorylated by rhodopsin kinase (RK), by the sequential attachment of one or more phosphates at its C-terminal serine and threonine residues (18). Then phosphorylated Rh* is capped by arrestin (Arr), which shuts it off by making it inaccessible for T (19–22). The catalytic activity of E* terminates when activated transducin dissociates from the complex T*·E after its intrinsic GTPase hydrolyzes GTP to GDP. This latter process is greatly accelerated by RGS9 (23).

Absolute sensitivity of the visual system is limited by dark noise due to isomerization of Rh by thermal fluctuations and spontaneous activation of E (1,6,7,24–26). The system is so sensitive that it can act, at least for dim flashes, as a photon counter (27), permitting one absorbed photon to be distinguished from two (4).

This high reproducibility of SPR is intriguing, as the process contains several elements of randomness. For example, the disk activated by a quantum of light is a random one among the 1000 disks forming the rod outer segment (ROS); and the activation site is random within the activated disk; Rh* randomly diffuses within the activated disk, and remains active at random time t_{Rh^*}. Finally, the number of Rh*-phosphorylations before quenching by arrestin is random.

Several hypotheses have been proposed to explain low SPR variability. Among these is that t_{Rh^*} has little effect on the process, that is, either t_{Rh^*} is itself little-variable, or the photocurrent is relatively insensitive to variations of t_{Rh^*} (8). Another is that a multistep Rh* shutoff stabilizes the output photocurrent (6,7,28).

It was pointed out in Pugh (10) that a full account of the single photon response has to include an analysis of the spatiotemporal diffusion of the second messengers cGMP and Ca^{2+} in the layered geometry of the ROS. This is the key point of this study. In a series of articles, we have created a mathematical and computational model of the spatiotemporal dynamics of cGMP and Ca^{2+} in the ROS by resolving the layered geometry. This was done by means of the mathematical theories of homogenization and concentrated capacity (13–15,29,30). The model is a tool that permits one, in almost real-time, to separate and check the effects of all the biochemical and physical parameters involved, even the random ones, including diffusivities, reaction rates, catalytic coefficients, and shutoff times. The geometrical parameters of the ROS including disk incisures, their shape, and their geometrical arrangements, can also be varied and their effects on the response can be calculated.

By means of this model, we separate and test the effects of the various random events contributing to the variability of the response. These include the random activation site, the random walk of Rh*, and the hypotheses of a multistep or abrupt random shutoff of Rh*.

We find that neither a random activation site nor a random walk of Rh* contribute significantly to the CV of E*; it is the multistep Rh* inactivation mechanism that is the main contributor to the CV. However, the number of steps in deactivation is not a main contributor to variability suppression. The surprising result of the simulations is that the diffusion of cGMP and Ca^{2+} damp out the variability of the SPR.

THE MATHEMATICAL MODEL

The dynamics of the second messengers cGMP and Ca^{2+} is modeled by taking the homogenized-concentrated limit of their physical, pointwise dynamics within the interdiscal spaces and in the outer shell. The limiting homogenized geometry is simpler in that the outer shell and the disks disappear and are replaced by dynamic equations on their limiting geometries, linked by equations expressing their mutual balance of fluxes. In particular, incisures in the homogenized-concentrated limit tend to segments $\mathcal{V}_j$ (Fig. 1). We denote by D_R the disk of radius R and by D_{eff} the effective domain of the

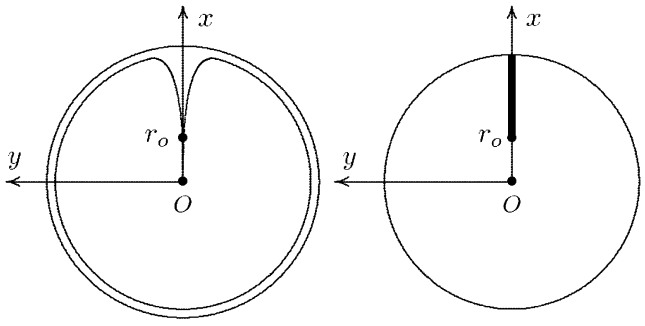

FIGURE 1 (*Left*) Transversal cross section of the ROS bearing an incisure. (*Right*) Limit of such a cross section, bearing the limiting incisure $\mathcal{V}$.

activation cascade—that is, D_R from which all the segments $\mathcal{V}_j$ have been removed:

$$D_{eff} = D_R - \bigcup_{j=1}^{m} \mathcal{V}_j.$$

We refer the reader to the literature (29,30) for the underlying mathematical analysis needed to compute such a homogenized-concentrated limit, and to the literature (13,15) for its biophysical significance. In Appendix A, we report the mathematical weak formulation of such a homogenized model, mainly to point out that

1. It is the starting point to writing a finite-elements code; and
2. It does not depend on the modeling of the activation cascade.

Indeed the function $(x, y, t) \to E^*(x, y, t)$ for (x, y) ranging over an activated disk, serves as an input only, and its dynamic can be modeled independently. In this respect, the dynamics of the second messengers cGMP and Ca^{2+} is a module of the visual transduction cascade and the dynamics of the activated effector E* is a separate module.

Dynamics of the activation cascade

A molecule of rhodopsin, activated at time $t = 0$, becomes inactivated abruptly, after a random time t_{Rh^*}, of average τ_{Rh^*}. During the random interval $[0, t_{Rh^*})$, however, Rh* goes through n molecular states Rh^*_j, $j = 1,\ldots, n$, each with transducin-activation rate ν_j, which remains constant as long as Rh* remains in the state Rh^*_j. For example, Rh^*_j might be in different phosphorylated states of Rh*, identified by the number $(j - 1)$ of phosphates attached to Rh* by RK. The state $(n + 1)$ is identified with Rh* being quenched by Arr binding. The transitions from the state j to $(j + 1)$ occur at random transition times $0 < t_j \le t_n = t_{Rh^*}$, with ν_j remaining constant during the time interval $(t_{j-1}, t_j]$, for $j = 1, \ldots, n$, and where $t_o = 0$. Denote by $\delta_{\mathbf{x}(t)}$ the Dirac mass in $\mathcal{R}^2$, concentrated at $\mathbf{x}(t) = (x(t), y(t))$, and dimension μm^{-2}, and by $\chi_{(t_{j-1},t_j]}$ the characteristic function of the interval $(t_{j-1}, t_j]$. Then the rate equations for T* and E* are

$$\begin{aligned}[T^*]_t - D_T\Delta[T^*] &= \sum_{j=1}^{n} \nu_j \chi_{(t_{j-1},t_j]}(t)\delta_{\mathbf{x}(t)} - k_{T^*E}[E][T^*] \\ [E^*]_t - D_E\Delta[E^*] &= k_{T^*E}[E][T^*] - k_{E^*}[E^*],\end{aligned} \quad (1)$$

weakly in $D_{eff} \times (0, T]$ (Appendix A), complemented by the initial data and the no-flux boundary conditions on ∂D_{eff} as

$$\begin{aligned}&[T^*](0) = [E^*](0) = 0 \quad \text{and} \\ &\nabla_{(x,y)}[T^*] \cdot \mathbf{n} = \nabla_{(x,y)}[T] \cdot \mathbf{n} = 0 \\ &\nabla_{(x,y)}[E^*] \cdot \mathbf{n} = \nabla_{(x,y)}[E] \cdot \mathbf{n} = 0\end{aligned}, \quad (2)$$

where $\mathbf{n}$ is the outward unit normal to ∂D_{eff}, which is well defined except at the extremities of the limiting incisures $\mathcal{V}_j$. It is assumed that the diffusivity of T and E is the same as that of their activated states. Thus, $D_T = D^*_T$ and $D_E = D^*_E$. In the dark, T* and E* are uniformly distributed in D_{eff}, with constant concentrations [T](0) and [E](0), respectively. At all $(x, y) \in D_{eff}$ and for all times, [E](0) is distributed into its active and inactive form, i.e.,

$$[E](x, y, t) + [E^*](x, y, t) = [E](0).$$

These stipulations and Eqs. 1 and 2 imply the conservation of mass,

$$\begin{aligned}E_{tot} = &\int_{D_{eff}} [E](x, y, t)dxdy + \\ &\int_{D_{eff}} [E^*](x, y, t)dxdy = \pi R^2[E](0).\end{aligned} \quad (3)$$

In Eq. 1, the constant k_{T^*E} is the rate of formation of the T*·E complex or equivalently the rate of formation of E*. The constant k_{E^*} is the rate of deactivation of E* by the hydrolysis of GTP by T*, within the T*·E complex. The constant k_j, in s^{-1}, is the constant of activation of T* by Rh* through a successful encounter at time t at the position $\mathbf{x}(t)$ on the random path of Rh*. The activation rate is proportional to the relative number ([T] – [T*])/[T] of transducin molecules available for activation. It is assumed that $T^*(x,y,t) \ll [T](x,y,t)$ at all $(x, y) \in D_{eff}$, and at all times, so that local depletion of T is negligible, which is true for dim light responses including SPR. Alternatively, at bright light the activation process obeys Michaelis-Menten kinetics with Michaelis constant K, and activation occurs in the saturation limit, i.e.,

$$t \in (t_{j-1}, t_j] \to k_j \frac{[T]}{[T] + K}\delta_{\mathbf{x}(t)} \approx k_j\delta_{\mathbf{x}(t)} \quad \text{for} \quad [T] \gg K.$$

Models like Eq. 1 involve deterministic parts, such as the diffusion processes appearing on the left-hand side, deterministic first-order reactions with given rates, and stochastic terms. Indeed, the transitions times t_j for $j = 1,\ldots, n$ are random variables, and the path $t \to \mathbf{x}(t)$ is random.

STATISTICS AND BIOCHEMISTRY

A newly created Rh* is in the state 1 (denoted by Rh^*_1). It undergoes a transition to the state 2 after some time s_1, which is an exponentially distributed random variable with mean τ_1. More generally, Rh* reaches the state j (denoted by Rh^*_j) after $(j - 1)$ transitions from Rh^*_1. Then it undergoes a transition to the state $(j + 1)$ after time s_j has elapsed from the birth of Rh^*_j. The quantity s_j is an exponentially distributed random variable with mean τ_j. After n transitions, Rh* is turned off, reaching the state $n + 1$. The random variables $s_1, \ldots, s_n$ are mutually independent; their sum, denoted by t_{Rh^*}, is the lifespan of Rh*, which itself is a random variable with mean τ_{Rh^*}. The s_j are connected to the transition times $t_j = \sum_{h=1}^{j} s_h$, and their mean values must satisfy

$\sum_{j=1}^{n} \tau_j = \tau_{Rh^*}$. The theoretical calculation of the probabilities $P_j(t)$ of Rh* being in the j^{th} state at time t, hinges upon the structure of the sequences of the mean times $\{\tau_1, \ldots, \tau_n\}$, and the catalytic constants $\{\nu_1, \ldots, \nu_n\}$. The structure of such sequences in turn depends on the underlying biochemistry. A theoretical choice could be that τ_j and ν_j are the same in each state. More biochemically motivated choices would allow for a $\{\tau_j\}$ and $\{\nu_j\}$ to be variable from state to state. The CV of some quantities can be computed theoretically, a priori, in terms of the sequences $\{\nu_j\}$ and $\{\tau_j\}$ irrespective of their structure (Appendix B). We will return to these explicit formulae in Eq. 14, to discuss their biochemical significance.

Biochemical sequences $\{\tau_j\}$ and $\{\nu_j\}$

Experimental evidence suggests that the phosphorylated states Rh_j^* are functionally different (31). In particular, their ability to activate T is different (32,33).

Shutoff of Rh* occurs by phosphorylation by RK, followed by Arr binding. Like many G-protein coupled receptors, rhodopsin contains multiple sites for phosphorylation in its C-terminus. The contribution of various phosphorylation sites to Rh* interaction with T, RK, and Arr has been addressed by several investigators, in a series of in vitro experiments (32,34–38). Biochemical experiments using the competition of synthetic phosphorylated and unphosphorylated rhodopsin C-terminal peptides suggest that phosphorylation of rhodopsin by RK is a cooperative process, i.e., the incorporation of one or two phosphates increases the probability of further phosphorylation (35). This phenomenon was rationalized in terms of increased affinity of the substrate for RK with increased phosphorylation (35). This should tend to favor the formation of multiphosphorylated rhodopsin species. Another study using full-length proteins (39) came to the opposite conclusion: that phosphorylation of rhodopsin and/or autophosphorylation of RK progressively decreases its affinity for light-activated rhodopsin. This mechanism could favor the accumulation of Rh* species with low level of phosphorylation. These models predict very different outcomes at high levels of illumination, when the number of Rh* molecules is comparable to the number of RK molecules in the photoreceptor, creating conditions where Rh* molecules compete for RK. However, under conditions relevant for our analysis where single photon responses are recorded, i.e., in the dark-adapted rod with only one Rh* and ≈200,000 molecules of RK (16), the difference between the predictions of these two models is negligible.

There is no consensus in the literature regarding the quantitative effect of progressive rhodopsin phosphorylation on transducin activation and arrestin binding (18,32,33). We based our choice for the sequences $\{\tau_j\}$ and $\{\nu_j\}$ on the data obtained with chromatographically separated rhodopsin species with different levels of phosphorylation (18,32), rather than on results obtained with complex mixtures of different phosphorhodopsin species (33). The catalytic activity of Rh* decreases with increasing levels of phosphorylation, at a rate of ~12% for each additional level of phosphorylation (Fig. 2 in (32)). Thus,

$$\nu_j = \nu_{RG} e^{-0.12(j-1)}, \quad \text{for} \quad j = 1, \ldots, n, \tag{4}$$

where ν_{RG} is the catalytic activity of Rh*, and j is the level of phosphorylation. The mean resting times τ_j are assumed to be equal, except for the first, nonphosphorylated state. The first resting time τ_1 is longer, as several biochemical processes have to occur before the first phosphorylation. At dark concentrations of Ca^{2+}, recoverin is in the Ca^{2+}-bound form at the membrane, and forms a complex with RK, blocking its activity (16). As $[Ca^{2+}]$ drops, recoverin releases Ca^{2+}, and dissociates from RK, which permits the phosphorylation of Rh* (16,34). For the mouse it is reported in Mendez et al. (40) that Rh* remains in its unphosphorylated state, for ~100 ms or $\sim 1/2 t_{peak}$, and then it deactivates in two or three states, each of comparable length, with decreasing catalytic constants. A recent study (23) provided definitive proof that the observed dominant time constant of recovery (t = 200 ms) reflects RGS9-assisted GTP hydrolysis by transducin α-subunit. Increasing expression of RGS9 in rods progressively reduces this constant. However, eventually the constant reaches a new limit, 80 ms, beyond which further increases in RGS9 expression could not reduce it, indicating that some other step became rate-limiting (23). The molecular nature of this second-slowest step has not been identified. It could be the maximum catalytic rate of transducin-RGS9 complex, the rate of the release of PDE from T-GDP, the rate of rebinding of PDE to PDE, or the rate of rhodopsin inactivation. However, this time constant determines the upper limit of

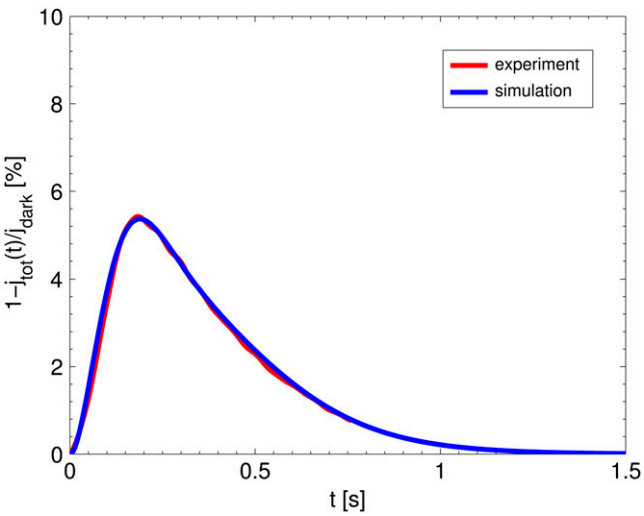

FIGURE 2 The red curve reports the average of an extensive set of experimental SPR responses for mouse, kindly provided to us by F. Rieke. The blue curve is our numerical simulation of the mouse SPR using the mathematical model of Appendix A for the set of parameters in Table 3. The agreement is excellent, thereby showing that this selection parameters accurately reflects the timecourse and amplitude of experimentally generated light responses.

the Rh* lifetime, which includes sequential phosphorylation by RK to appropriate level (18) and arrestin binding. Taking this information into account, we choose

$$\tau_1 = \frac{\tau_{\mathrm{Rh}^*}}{2}, \quad \tau_j = \frac{\tau_{\mathrm{Rh}^*}}{2(n-1)}, \quad \text{for} \quad j = 2, \ldots, n. \quad (5)$$

Simulations for these choices of $\{\tau_j\}$ and $\{\nu_j\}$ are referred to in captions and legends as nonequal times and nonequal catalytic rates (NN). Relative length of the steps that reflect rhodopsin phosphorylation by RK and of the last step that involves arrestin binding depends on the concentrations of RK and arrestin in the outer segment (OS) in the dark (SPR is recorded in fully dark-adapted animals). RK concentration was recently estimated at 12 μM (16). The estimates of the amount of arrestin present in the OS in the dark vary from 1–3% (41,42) to <7% of the total (43). The estimated rhodopsin concentration in the OS is ~3 mM (16) and arrestin is expressed at 0.8:1 ratio to rhodopsin (42,43). So if 1, 2, 3, or 7% of arrestin is present in the OS in the dark, it translates into 24, 48, 72, or 168 μM concentrations, which at first glance look very different. However, based on the self-association constants (44), one can calculate that at any of these concentrations a significant proportion of arrestin would be in the form of dimer and tetramer, with ~45, 30, 22, and 14%, respectively, being a monomer, which is the only form of arrestin capable of binding rhodopsin (44). This yields the concentrations of the active monomer in dark-adapted OS of 11, 14, 16, and 23 μM, respectively. Thus, the concentrations of active RK (after the decrease of Ca^{2+} removes recoverin-mediated brake) and of active arrestin monomer are comparable. Therefore the length of the last step (between the last phosphorylation and arrestin binding) can be assumed to be close to the lengths of the preceding phosphorylation steps, with the exception of step 1 (unphosphorylated Rh*), which is longer.

Sequence for which $\tau_j\nu_j$ = const

This choice is often made (6,7,9,45,46), although it is purely theoretical and is not motivated by known biochemistry. Let E** denote the random total number of molecules of E* produced over the entire time duration of the process, after a single isomerization. In Appendix B, a theoretical formula has been derived for CV(E**), regardless of the structure of the sequences $\{\tau_j\}$ and $\{\nu_j\}$ (Eq. 15). This equation implies that if $\nu_j\tau_j = \text{const}$ for all $j = 1, \ldots, n$, then

$$CV(\mathrm{E}^{**}) = \frac{1}{\sqrt{n}}, \text{ for sequences for which } \nu_j\tau_j = \text{const}. \quad (6)$$

A CV of the order of $1/\sqrt{n}$ has been reported in several contributions (6,7,9,46), although it was not precisely defined to which function it relates (molecules of E*, lowest cGMP concentration, peak current, or something else). To compare our approach with the existing literature, we have performed simulations for sequences $\{\nu_j\}$ and $\{\tau_j\}$ satisfying Eq. 6 and for which, in addition,

$$\nu_j = \nu_{\mathrm{RE}} \quad \text{and} \quad \tau_j = \frac{t_{\mathrm{Rh}^*}}{n} \quad \text{for all} \quad j = 1, \ldots, n. \quad (7)$$

This stipulates that the phosphorylated states of Rh* last, on average, an equal amount of time t_{Rh^*}/n, and that the catalytic rates ν_j are the same in each state. Simulations for these choices of $\{\tau_j\}$ and $\{\nu_j\}$ are referred to in captions and legends as equal times and equal catalytic rates (EE). To be sure, Eq. 6 is satisfied by infinitely many choices of $\{\nu_j\}$ and $\{\tau_j\}$ for which neither ν_j nor τ_j is constant, but their product is (See More on statistics and biochemistry in Appendix B).

RANDOM EVENTS CONTRIBUTING TO SPR VARIABILITY

A code for Eq. 1 presents two major difficulties. The first is the incised geometry of D_{eff}, which is dealt with by mathematical methods of numerical analysis. The second is the stochastic input on the right-hand side of the first equation in Eq. 1. This includes the random activation site, the random path of Rh*, and random shutoff mechanism. The model permits one to test independently the effects of these random components on the variability of the response. For example, one can separate the effects of the activation site and the subsequent random walk of Rh* on D_{eff} from the shutoff mechanism. Also, one can separate the effects of the shutoff mechanism from the Brownian motion of Rh*. To achieve this, we performed the following sets of simulations:

Case 1

Fix the activation site $\mathbf{x}_o \in D_{\mathrm{eff}}$ and let Rh* follow its random Brownian path $t \to \mathbf{x}(t)$ starting at $\mathbf{x}(0) = \mathbf{x}_o$, with a prescribed second moment of its probability density. The shutoff time t_{Rh^*} and the number n of states before ultimate quenching, are fixed. The mean half-lives of different states could be equal or different, and still deterministically fixed. It turns out that if one regards the activation site as random, its mean position is at distance 2/3 of the radius of the activated disk. Thus, in this case, $|x_o| = \frac{2}{3}R$. The only random effect in this case is that of the Brownian motion of Rh*.

Case 2

The activation site $\mathbf{x}_o$ is random and Rh* remains fixed at its initial location. The shutoff time t_{Rh^*} and the number n of steps before quenching are fixed. The only randomness is the position of the activation site, which discriminates responses from each other.

Case 3

The activation site $|x_o| = \frac{2}{3}R$ is fixed and also Rh* remains fixed at x_o. Quenching of Rh* occurs at the random shutoff

time t_{Rh^*}, in n states. Random numbers τ_j are selected according to their exponential distribution and subject to either the statistic of Eq. 5 or 7, and the probabilities $P_j(t)$, for $j = 1, \ldots, n$, are computed accordingly (Appendix B). These simulations separate the random effects of the shutoff mechanism from those of the activation sites and the motion of Rh*.

Case 4

All the previous components are random (activation site, random path of Rh*, random shutoff time t_{Rh^*} for a given number of steps). This is the biologically realistic case, although the previous cases extract the impact of each component of randomness.

FUNCTIONALS DETECTING THE SPR VARIABILITY

A MATLAB-based, finite-element code has been written for the system in Eqs. 1–3, based on its weak formulation (Appendix A). The output E*, as a function of the two variables $(x, y) \in D_{eff}$ and time t, is then fed into the code for the homogenized system describing the dynamics of the second messengers (Appendix A). Finally, local and global currents generated across the ROS lateral surface, are computed by the formulae

$$J_{ex} = \frac{j_{ex}^{sat}}{\Sigma_{rod}} \frac{[Ca^{2+}]}{K_{ex} + [Ca^{2+}]}, \quad J_{cG} = \frac{j_{cG}^{max}}{\Sigma_{rod}} \frac{[cGMP]^{m_{cG}}}{K_{cG}^{m_{cG}} + [cGMP]^{m_{cG}}}. \quad (8)$$

In the first of these, j_{ex}^{sat} is the saturated exchange current (as $[Ca^{2+}] \to \infty$), K_{ex} is the Ca^{2+} concentration at which the exchange rate is half-maximal, and Σ_{rod} is the surface area of the lateral boundary S_ε of the ROS. In the second, j_{cG}^{max} is the maximal cGMP-current (as $[cGMP] \to \infty$), m_{cG} is the Hill exponent, and K_{cG} is the binding affinity of each cGMP binding site on the channel. Notice that J_{ex} and J_{cG} are current densities (i.e., current per unit area, measured in $pA/\mu m^2$), and, in general, have different values at different points of the lateral boundary S_ε of the ROS. In the absence of light, J_{ex} and J_{cG} are constant and equal to their constant, dark values $J_{ex;dark}$ and $J_{cG;dark}$ defined as in Eq. 8 with $[Ca^{2+}]$ and [cGMP] replaced by $[Ca^{2+}]_{dark}$ and $[cGMP]_{dark}$, respectively. Introduce cylindrical coordinates (θ, z) on the outer shell S_ε where z ranges over $(0, H)$ and θ ranges over $[0, 2\pi)$. The local value of (total) current density J_{loc} and its dark value J_{dark} are defined as

$$J_{loc}(\theta, z, t) = J_{ex}(\theta, z, t) + J_{cG}(\theta, z, t), \quad J_{dark} = J_{loc}|_{t=0}. \quad (9)$$

The corresponding global quantities are defined as integrals over the lateral boundary of the ROS, i.e.,

$$j_{tot}(t) = \int_{\Sigma_{rod}} J_{loc}(\theta, z, t) dS, \quad j_{dark} = j_{tot}|_{t=0}, \quad (10)$$

where dS is the surface measure of the lateral boundary of the ROS.

While $J_{loc}(\theta, z, t)$ is pointwise current defined on the outer shell, experimentally what is measured is the global current $j_{tot}(t)$ as a function of time, and what is graphed is the relative local or global current drop,

$$1 - \frac{J_{loc}(\theta, z, t)}{J_{dark}}, \quad 1 - \frac{j_{tot}(t)}{j_{dark}}. \quad (11)$$

The variability of the SPR will be analyzed by measuring the variability of the effector and the photocurrent separately and then by comparing them. The natural variable functionals of the effector E* are

$E^*(t) = \int_{D_{eff}} [E^*](x, y, t) dx dy$	Total # of molecules of E^* in D_{eff} at time t.
$E^{**}(t) = \int_0^t E^*(s) ds$	Total activity of E^* up to time t.
$E^{**} = \int_0^\infty E^*(t) dt$	Total activity of E^* over entire lifetime of the process.
t^*_{peak}	Time to peak of $E^*(t)$.
$E^*(t^*_{peak})$	Peak value of $E^*(t)$. (12)

The last three are scalar quantities and their CV is reported in Table 1. The first two are functions of time. The CV of the second, as a function of time, will be reported in Fig. 3, *A* and *C*, and Fig. 4, *A* and *C*. The natural variable functionals of the photocurrent are

$I(t) = 1 - \frac{j_{tot}(t)}{j_{dark}}$	Total (relative) current suppression at time t.
$I^*(t) = \int_0^t I(s) ds$	Total (relative) charge suppression up to time t.
$I^{**} = \int_0^\infty I(t) dt$	Total (relative) charge suppression over timecourse of the phenomenon.
t_{peak}	Time to peak of $I(t)$.
$I(t_{peak})$	Peak value of $I(t)$. (13)

While the last one is a consequence of the first, we have listed it separately since this is the experimental quantity actually being measured (6–8). The last three are scalar quantities and their CV is tabulated in Table 2. The first two are functions of time. The CV of the second is graphed as a function of t in Fig. 3, *B* and *D*, and Fig. 4, *B* and *D*. The quantity I** is the total relative charge produced over the entire timecourse of the phenomenon after isomerization by a single photon. In Field and Rieke (28) it is argued that the "...area captures fluctuations occurring at any time during the response, and thus provides a good measure of the total extent of response fluctuations...". Pointwise fluctuations are tracked by $I(t)$ and $I^*(t)$. The very same quantity I**, when normalized by

TABLE 1 CV (σ/μ) for E, E*(t^*_{peak}), and t^*_{peak}**

				E**				E*(t^*_{peak})				t^*_{peak}			
Mech.	Species	Incisure	Case	2	3	4	5	2	3	4	5	2	3	4	5
NN	Mouse	N	1	0.00	0.00	0.00	0.00	0.00	0.00	0.00	0.00	0.00	0.00	0.00	0.00
			2	0.00	0.00	0.00	0.00	0.00	0.00	0.00	0.00	0.00	0.00	0.00	0.00
			3	0.70	0.60	0.61	0.61	0.42	0.38	0.39	0.39	0.68	0.55	0.52	0.49
			4	0.69	0.65	0.63	0.62	0.42	0.38	0.38	0.39	0.67	0.58	0.53	0.49
		Y	1	0.00	0.00	0.00	0.00	0.00	0.00	0.00	0.00	0.00	0.00	0.00	0.00
			2	0.00	0.00	0.00	0.00	0.00	0.00	0.00	0.00	0.00	0.00	0.00	0.00
			3	0.70	0.60	0.61	0.61	0.42	0.38	0.39	0.39	0.68	0.55	0.52	0.49
			4	0.69	0.65	0.63	0.62	0.42	0.38	0.38	0.39	0.67	0.58	0.53	0.49
	Salamander	N	1	0.00	0.00	0.00	0.00	0.00	0.00	0.00	0.00	0.00	0.00	0.00	0.00
			2	0.00	0.00	0.00	0.00	0.00	0.00	0.00	0.00	0.00	0.00	0.00	0.00
			3	0.71	0.61	0.62	0.62	0.61	0.53	0.54	0.53	0.69	0.57	0.55	0.54
			4	0.70	0.66	0.65	0.63	0.61	0.56	0.54	0.54	0.68	0.61	0.57	0.55
		Y	1	0.00	0.00	0.00	0.00	0.00	0.00	0.00	0.00	0.00	0.00	0.00	0.00
			2	0.00	0.00	0.00	0.00	0.00	0.00	0.00	0.00	0.02	0.01	0.00	0.00
			3	0.71	0.60	0.63	0.62	0.61	0.52	0.54	0.53	0.68	0.56	0.56	0.54
			4	0.70	0.66	0.63	0.63	0.61	0.56	0.53	0.53	0.67	0.61	0.56	0.54
EE	Mouse	N	1	0.00	0.00	0.00	0.00	0.00	0.00	0.00	0.00	0.00	0.00	0.00	0.00
			2	0.00	0.00	0.00	0.00	0.00	0.00	0.00	0.00	0.00	0.00	0.00	0.00
			3	0.70	0.57	0.48	0.45	0.42	0.36	0.32	0.29	0.69	0.55	0.47	0.43
			4	0.69	0.58	0.49	0.44	0.42	0.36	0.32	0.29	0.68	0.56	0.48	0.43
		Y	1	0.00	0.00	0.00	0.00	0.00	0.00	0.00	0.00	0.00	0.00	0.00	0.00
			2	0.00	0.00	0.00	0.00	0.00	0.00	0.00	0.00	0.00	0.00	0.00	0.00
			3	0.70	0.57	0.48	0.45	0.42	0.36	0.32	0.29	0.69	0.55	0.47	0.43
			4	0.69	0.58	0.49	0.44	0.42	0.36	0.32	0.29	0.68	0.56	0.48	0.43
	Salamander	N	1	0.00	0.00	0.00	0.00	0.00	0.00	0.00	0.00	0.00	0.00	0.00	0.00
			2	0.00	0.00	0.00	0.00	0.00	0.00	0.00	0.00	0.00	0.00	0.00	0.00
			3	0.71	0.58	0.49	0.45	0.61	0.50	0.43	0.40	0.68	0.56	0.47	0.44
			4	0.70	0.59	0.50	0.45	0.61	0.51	0.44	0.39	0.68	0.57	0.48	0.43
		Y	1	0.00	0.00	0.00	0.00	0.00	0.00	0.00	0.00	0.00	0.00	0.00	0.00
			2	0.00	0.00	0.00	0.00	0.00	0.00	0.00	0.00	0.00	0.00	0.00	0.00
			3	0.71	0.57	0.49	0.45	0.61	0.50	0.43	0.40	0.68	0.55	0.47	0.43
			4	0.70	0.58	0.50	0.45	0.61	0.51	0.43	0.39	0.67	0.56	0.47	0.43

NN, Shutoff of Rh* in n biochemical states of decreasing duration and catalytic activity (see Biochemical Sequences $\{\tau_j\}$ and $\{\nu_j\}$); *EE*, Shutoff of Rh* in n theoretical states of equal duration and equal catalytic activity (see Sequence for Which $\tau_j\nu_j = \text{Const}$); *Y*, Yes; and *N*, No.

the peak response amplitude $I(t_{peak})$, is referred to as integration time, and reported as a measure of variability in a number of articles (8,22,31,40,46–48).

PROCEDURES AND METHODS

The selection of one of the cases in Random Events Contributing to SPR Variability determines the right-hand side of the Eq. 1, and the corresponding biochemistry and statistics. Then the code computes the functions $D_{\text{eff}} \ni (x, y) \rightarrow E^*(x, y, t)$ at each time $t \geq 0$, the currents in Eqs. 8–11, via [cGMP] and $[Ca^{2+}]$, and then the local and global relative drops (Eq. 10). After a large number of these numerical experiments ($\sim$1000), one computes the mean, the standard deviation, and the CV of the functionals indicated in Functionals Detecting the SPR Variability.

Each of these numerical experiments is carried for ROS with incisures and without incisures, as a way of investigating their functional role. A comparative analysis has been conducted for salamander and mouse, following the experimental results of Rieke and Baylor (6) for amphibians, and of Field and Rieke (28) for mammals.

Finally the simulations are run with clamped calcium, to test the hypothesis put forth in the literature (6,8,46) that calcium feedback does not affect the variability of SPR.

Parameters

For the salamander, a reasonably complete set of parameters has been compiled in the literature (14,15). In Table 3, we have generated a complete, self-consistent set of parameters for the mouse ROS, partly taken from the literature, partly generated by comparative consideration with other higher vertebrate (bovine), and partly computed from the experimental data for mouse SPR kindly provided by Dr. F. Rieke. We discuss here a few points related to the choice of these parameters. The parameters used in the model of the diffusion of Ca^{2+} and cGMP in the cytosol (see Weak Formulation of the Dynamics of cGMP, and Weak Formulation of the Dynamics of Ca^{2+}) are taken from the literature (14,15).

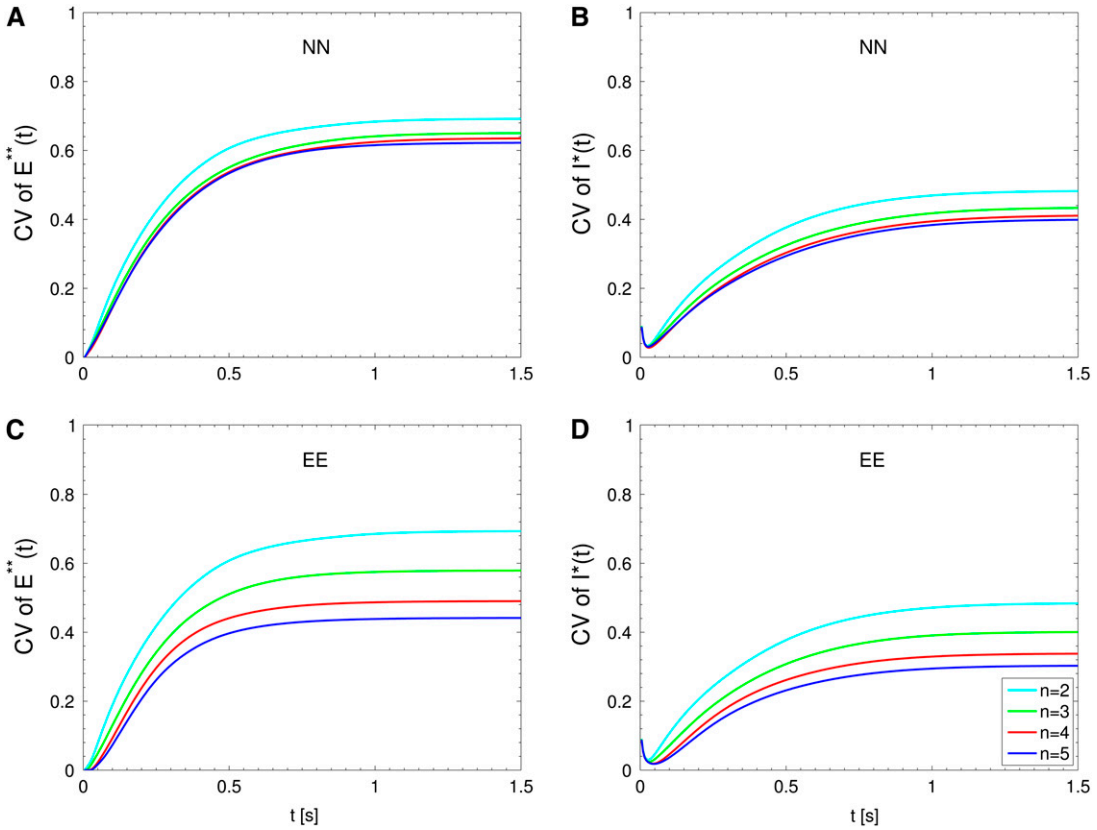

FIGURE 3 Mouse: comparing the CV of the total activated effectors $E^{**}(t) = \int_0^t E^*(s)ds$ at time t with the CV of the total relative charge $I^*(t) = \int_0^t I(s)ds$ up to time t. (*NN*) Shutoff of Rh* in n biochemical states of decreasing duration and catalytic activity (see Biochemical Sequences $\{\tau_j\}$ and $\{\nu_j\}$). (*EE*) Shutoff of Rh* in n theoretical states of equal duration and equal catalytic activity (see Sequence for Which $\tau_j\nu_j = \text{Const}$). All simulations assume all activation steps as random (Case 4 of Random Events Contributing to SPR Variability). In all cases, CV decreases with increasing n. (*A* and *B*) For the biochemical state NN, the CV of both $E^{**}(t)$ and $I^*(t)$ stabilizes asymptotically after 3–4 phosphorylated states. A CV of ~60% for $E^{**}(t)$ at times past the peak time is reduced to a CV of ~40% for the corresponding photocurrent $I^*(t)$. (*C* and *D*) For the theoretical state EE, increasing n gives in all cases a decreased CV although at a decreasing rate for increasing n. The CV comparison $E^{**}(t)$ (~60%) to $I^*(t)$ (~40%) is still present, thus pointing to an intrinsic variability reduction effect of the diffusion part of the process.

There is considerable uncertainty about the parameters appearing in Eq. 1, and describing the diffusion of E* and T* in the activated disk. These include surface diffusion coefficients D_{E^*} and D_{T^*} of activated effector and transducin; the rate-constant k_E of inactivation of E* through the activation of RGS9 to stimulate the GTP hydrolysis of T*; the rate k_{T^*E} of activation of E* by G*; and the constants k_j, for $j = 1, \ldots, n$, which are the rates of activation of G* by Rh*. Finally, though not explicitly appearing in Eq. 1, two more parameters are needed in the model: the diffusivity and the average lifetime of activated rhodopsin.

The parameter k_E is the inactivation rate of the G*·E* complex, and identifies the dominant time constant $\tau_E = 1/k_E$, in the recovery process. That is, τ_E is the time constant for inactivation of the G*·E* complex. For salamander, it is reported to be $\tau_E \approx 1.5$ s (49,16). In the simulations, we have taken $k_E \approx 0.64\ s^{-1}$ as in Nikonov et al. (49).

Let $D^o_{Rh^*}$, $D^o_{T^*}$, and $D^o_{E^*}$ denote the surface diffusion coefficients of Rh*, G*, and E*, on the activated disks. The value of these parameters has been estimated in Pugh and Lamb (17), both for amphibians and mammals. The diffusion theory put forth in Pugh and Lamb (17) is based on the simplifying assumption that both Rh* and E* remain still, while G* diffuses. In Caruso et al. (15), we adapted this approach, by selecting E* as the only mobile species. The advantage is that the reaction diffusion system describing the motion of G* and E* can be replaced by a single equation, for [PDE*], where the reaction term due to the presence of Rh* appears as a fixed source. This, however, would lead to underestimating the overall activation of E, since this reaction is essentially diffusion-controlled. To compensate for this unwanted effect, we augment the diffusion coefficient of the activated effector by replacing it with the sum of the three diffusivities, $D^o_{Rh^*}$, $D^o_{T^*}$, and $D^o_{E^*}$. This compensation mechanism is analogous to a similar argument in Pugh and Lamb (17). Notice that the choice of these parameters has to discriminate between Cases 1 and 4, and Cases 2 and 3. In the latter group of simulations, we continue to assume that Rh*

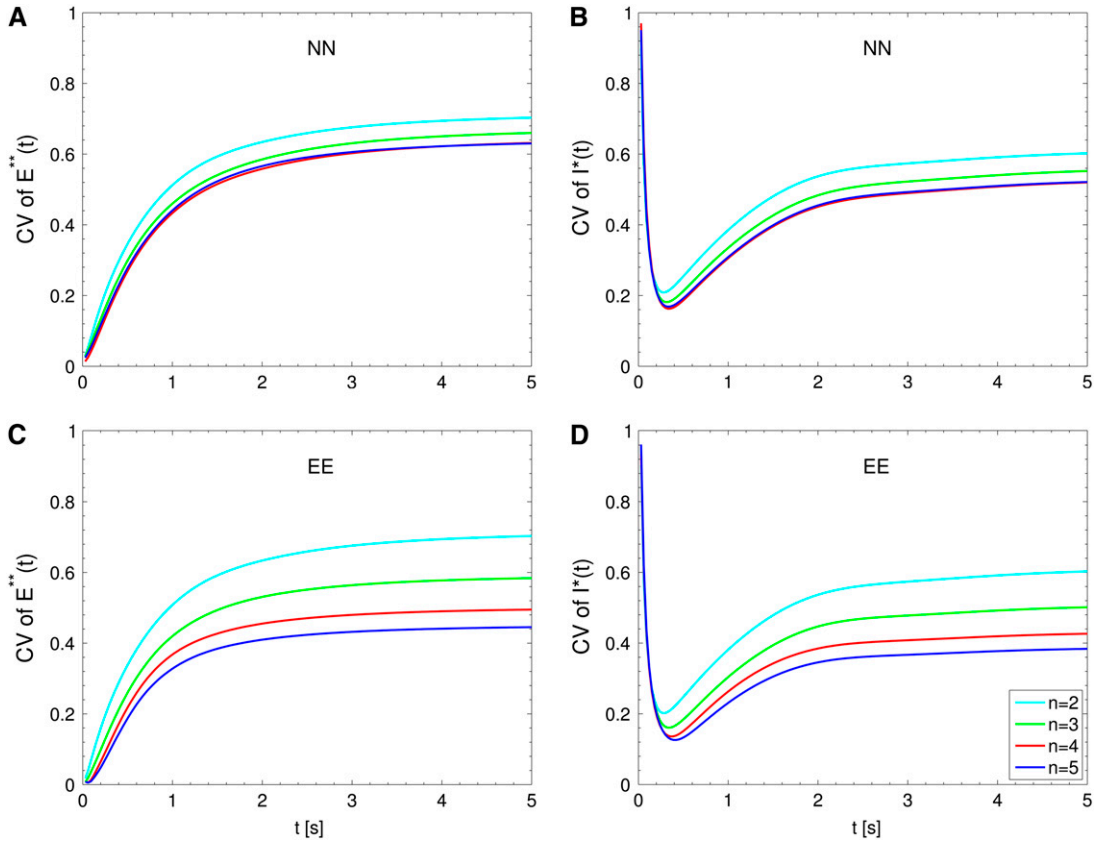

FIGURE 4 Salamander: comparing the CV of the total activated effectors $E^{**}(t) = \int_0^t E^*(s)ds$ at time t with the CV of the total relative charge $I^*(t) = \int_0^t I(s)ds$ up to time t. (*NN*) Shutoff of Rh* in n biochemical states of decreasing duration and catalytic activity (see Biochemical Sequences $\{\tau_j\}$ and $\{\nu_j\}$); (*EE*) Shutoff of Rh* in n theoretical states of equal duration and equal catalytic activity (see Sequence for Which $\tau_j\nu_j = \text{Const}$). All simulations assume all activation steps as random (Case 4 of Random Events Contributing to SPR Variability). In all cases, CV decreases with increasing n. For NN, the CV stabilizes for $n \geq 3$ and it is essentially the same for $n = 3, 4, 5$. For EE, the CV keeps decreasing with increasing n, although at a decreasing rate for increasing n. For the salamander at early times, the CV is initially large and then rapidly drops. No similar effect occurs in mouse. (*A* and *B*) For the biochemical state NN, the CV of both $E^{**}(t)$ and $I^*(t)$ stabilizes asymptotically after 3–4 phosphorylated states. A CV of ~60% for $E^{**}(t)$ at times past the peak time is reduced to a CV of ~50% for the corresponding photocurrent $I^*(t)$. (*C* and *D*) For the theoretical state EE, increasing n gives in all cases a decreased CV although at a decreasing rate for increasing n. The CV comparison $E^{**}(t)$ (~60%) to $I^*(t)$ (~50%) is still present, thus pointing to an intrinsic variability reduction effect of the diffusion part of the process. The suppression of CV for the photocurrent $I^*(t)$ with respect to CV of the activating $E^{**}(t)$, while present, is less dramatic than for mouse (Fig. 3, *A* and *B*). In addition, we observe a sharp variability at early times, which is likely due to presence of the incisures and their distributed geometry. This is supported by the absence of such incipient CV, in lumped models insensitive to incisures geometry (see also captions of Fig. 5). This early-time high CV seems also to be due to the random position of the activation site. Indeed, photons absorbed close to the disk boundary, yield a faster response than those absorbed far away from the boundary, say near the center of the disk. After a short time, depending on the diffusivity coefficients on the disk and on the disk radius, this difference is reduced. In the mouse, where diffusivities are larger and the radius is smaller than similar parameters in the salamander, no significant increase of variability at early times is observed (see also Fig. 3).

remains fixed, but the activation and diffusion of transducin is taken explicitly into account. For this reason, as in the literature (15,17), the diffusion coefficient for G* is taken as the sum of $D^o_{Rh^*}$ and $D^o_{T^*}$, and no correction is required in the remaining part of the cascade. Thus, in Eq. 1, one has $D_{T^*} = D^o_{Rh^*} + D^o_{T^*}$ and $D_{E^*} = D^o_{E^*}$. Instead, in Cases 1 and 4, the simplifying assumption that Rh* stays still is dropped, and we account for each reaction diffusion step in the cascade separately. Then, each diffusion coefficients is set equal to its experimentally estimated value (17). Thus, in particular, $D_{E^*} = D^o_{E^*}$ and $D_{T^*} = D^o_{T^*}$.

The diffusivity of rhodopsin, although it does not appear explicitly in Eq. 1, is used in generating a random walk of the activated molecule. A second hidden parameter is the mean τ_{Rh^*}, of the random lifetime t_{Rh^*} of Rh*. Although the general scheme of rhodopsin inactivation has been well established in vitro and is widely used as a paradigm for the inactivation of a larger family of G-protein-coupled receptors, there are no conclusive experimental measurements of the timecourse of Rh* inactivation in vivo. For salamander, Lyubarsky et al. (50) have argued that the inactivation time constant of Rh* is ~0.4 s. For mouse, Lyubarsky and Pugh

TABLE 2 CV (σ/μ) for I, I(t_{peak}), and t_{peak}**

					I**				I(t_{peak})				t_{peak}			
Mech.	Species	Model	Incisure	Case	2	3	4	5	2	3	4	5	2	3	4	5
NN	Mouse	SR	N	3	0.46	0.39	0.39	0.38	0.24	0.20	0.20	0.19	0.17	0.15	0.14	0.16
				4	0.46	0.41	0.39	0.38	0.25	0.21	0.19	0.19	0.17	0.20	0.19	0.15
			Y	3	0.48	0.41	0.41	0.40	0.27	0.23	0.23	0.22	0.24	0.17	0.18	0.19
				4	0.48	0.43	0.41	0.40	0.28	0.24	0.22	0.22	0.24	0.20	0.18	0.19
		TWS	N	4	0.48	0.40	0.40	0.39	0.25	0.21	0.21	0.20	0.25	0.18	0.20	0.21
			Y	4	0.50	0.42	0.42	0.41	0.28	0.24	0.24	0.23	0.27	0.20	0.21	0.21
		GWS		4	0.63	0.54	0.55	0.54	0.43	0.39	0.39	0.39	0.38	0.29	0.28	0.26
	Salamander	SR	N	3	0.52	0.44	0.44	0.44	0.34	0.29	0.28	0.28	0.21	0.17	0.16	0.16
				4	0.54	0.49	0.48	0.46	0.43	0.39	0.38	0.38	0.21	0.19	0.18	0.18
			Y	3	0.60	0.51	0.52	0.51	0.46	0.39	0.40	0.39	0.21	0.18	0.17	0.16
				4	0.60	0.55	0.52	0.52	0.48	0.42	0.39	0.39	0.20	0.18	0.17	0.16
		TWS	N	4	0.64	0.55	0.56	0.56	0.50	0.44	0.44	0.44	0.26	0.20	0.19	0.19
			Y	4	0.66	0.57	0.58	0.58	0.53	0.47	0.47	0.47	0.27	0.21	0.20	0.19
		GWS		4	0.71	0.61	0.62	0.62	0.58	0.51	0.52	0.51	0.28	0.22	0.21	0.21
EE	Mouse	SR	N	3	0.47	0.38	0.32	0.29	0.24	0.19	0.17	0.15	0.18	0.16	0.17	0.15
				4	0.46	0.38	0.32	0.29	0.25	0.20	0.17	0.15	0.23	0.20	0.16	0.15
			Y	3	0.48	0.39	0.33	0.31	0.27	0.22	0.19	0.17	0.27	0.23	0.20	0.17
				4	0.48	0.40	0.34	0.30	0.28	0.22	0.19	0.17	0.26	0.23	0.17	0.17
		TWS	N	4	0.48	0.39	0.33	0.30	0.25	0.20	0.18	0.15	0.30	0.26	0.20	0.19
			Y	4	0.50	0.40	0.34	0.32	0.28	0.23	0.20	0.18	0.31	0.26	0.22	0.21
		GWS		4	0.63	0.51	0.44	0.40	0.44	0.37	0.33	0.31	0.38	0.30	0.24	0.22
	Salamander	SR	N	3	0.52	0.42	0.36	0.33	0.34	0.28	0.24	0.21	0.21	0.17	0.14	0.13
				4	0.54	0.45	0.39	0.35	0.43	0.37	0.33	0.32	0.21	0.18	0.16	0.15
			Y	3	0.60	0.49	0.42	0.39	0.46	0.39	0.33	0.31	0.21	0.18	0.15	0.14
				4	0.60	0.50	0.43	0.38	0.48	0.39	0.34	0.30	0.20	0.18	0.15	0.14
		TWS	N	4	0.64	0.52	0.45	0.41	0.50	0.42	0.37	0.34	0.27	0.21	0.17	0.16
			Y	4	0.66	0.54	0.46	0.43	0.53	0.45	0.39	0.36	0.27	0.21	0.17	0.16
		GWS		4	0.70	0.57	0.49	0.45	0.58	0.48	0.42	0.39	0.28	0.22	0.18	0.17

NN, Shutoff of Rh* in *n* biochemical states of decreasing duration and catalytic activity (see Biochemical Sequences $\{\tau_j\}$ and $\{\nu_j\}$); *EE*, Shutoff of Rh* in *n* theoretical states of equal duration and equal catalytic activity (see Sequence for Which $\tau_j\nu_j = \text{Const}$); *SR*, space-resolved; *TWS*, transversally well-stirred; *GWS*, globally well-stirred; *Y*, Yes; and *N*, No.

(51) found the effective lifetime of Rh* is $\leq$0.21 s, and an estimate of 0.15 s was also reported. The most recent estimate, based on the assumption that when the deactivation of transducin is progressively accelerated by increasing expression of RGS9, the inactivation of Rh* becomes rate-limiting, yielded 80 ms as a half-life of Rh* (23). Based on data obtained in recordings of human ERGs, Hood and Birch et al. (52) have argued that the lifetime of Rh* is $\approx$2 s.

The parameter ν_1 on the right-hand side of the first part of Eq. 1 is referred to in the literature as ν_{RE}, that is, the rate of activation of effector per Rh*, bypassing the role of G*. The value of ν_{RE} has been extracted from the published data (16,49,53). This parameter would remain constant along the full activation-deactivation phases if the effects of the different functional species of Rh* were not accounted for.

The kinetic constant K_{T^*E} is the rate of formation of the T*·E complex, through which E* is generated. Leskov et al. reported an essentially 1:1 coupling between G* and PDE* (16,54). Thus, it is reasonable to assume $K_{T^*E} = 1\ \mu m^2\ s^{-1}/\#$ and $\nu_{RE} = \nu_{RG}$.

The numerical ranges of the parameters D_{T^*} and D_{E^*}, as well as k_j, k_{T^*E}, and k_E, and their choices in our simulations are collected in Tables 3 and 4.

The incisures have been simulated as follows:

Salamander. Twenty-three incisures symmetrically distributed along the edge of the disk. Each is an isosceles triangle, which starts from the edge with width 15 nm and runs radially toward the center of the disk with the height of 4.64 μm. The total area exposed by the incisures is 0.8 μm^2. These parameters have been taken from Olson and Pugh (55) and elaborated in Caruso et al. (15).

Mouse. One incisure, shaped as an isosceles triangle of base 0.2593 μm, height 0.2828 μm, and area 0.0367 μm^2. These values are taken from the literature (17,56,57) and are elaborated and justified in Caruso et al. (15).

Parameter calibration

The parameters are calibrated by least-square fitting of the simulated response current to the experimental data. In the calibration, it is assumed that Rh* is shut off exponentially in one step. When enforcing the multiple step shutoff for Rh*, in either the EE or NN mechanism, the simulation response currents diverge from the best-fitting curve. To keep the best fitting, we restore the simulation response current by slightly

TABLE 3 Parameters for the Mouse ROS

Symbol	Units	Definition	Range	Value	References
α_{max}	$\mu M\ s^{-1}$	Maximum rate of cGMP synthesis at low Ca^{2+} concentration.	76.5; 55.9	76.5	(70,71)
$\alpha_{max}/\alpha_{min}$	—	Suppression ratio of α from high to low Ca^{2+} concentration.	6.7–13.9	13.9	(70–72)
A_{inc}	μm^2	Area of the incisure.		0.0367	
β_{dark}	s^{-1}	Rate of cGMP hydrolysis by dark activated PDE.	1.5–10	2.9	(31,47,71)
B_{cG}	—	Buffering power of cytoplasm for cGMP.	1–2	1	(16,17,49)
B_{Ca}	—	Buffering power of cytoplasm for Ca^{2+}.	17.5–44	20	(49,61,64)
c_{GE}	—	Coupling coefficient from G* to E*.	<1	1	(16,54)
$[cGMP]_{dark}$	μM	Concentration of cGMP in the dark.	2–4	3.0748	(16,17,49,62,71–74)
$[Ca^{2+}]_{dark}$	nM	Concentration of Ca^{2+} in the dark.	200–670	436.2	(16,47,75–82)
D_{cG}	$\mu m^2\ s^{-1}$	Diffusion coefficient for cGMP.	–500	150	(14,55,59)
D_{Ca}	$\mu m^2\ s^{-1}$	Diffusion coefficient for Ca^{2+}.	15	15	(64)
D_{E^*}	$\mu m^2\ s^{-1}$	Diffusion coefficient for activated PDE.	1.2	1.2	(17)
D_{G^*}	$\mu m^2\ s^{-1}$	Diffusion coefficient for activated G protein.	2.2	2.2	(17)
D_{R^*}	$\mu m^2\ s^{-1}$	Diffusion coefficient for activated Rh.	1.5	1.5	(17)
ε	nm	Disk thickness.	14–17	14.5	(17,57,83)
η	nm	Volume/surface ratio.		7.25	
$\mathcal{F}$	$\mathcal{C}mol^{-1}$	Faraday's constant.	96,500	96,500	
f_{Ca}	—	Fraction of cGMP-activated current carried by Ca^{2+}.	0.06–0.17	0.06	(16,31,70,84,85)
H	μm	Height of ROS.	20–24	23.6	(16,57,86,87)
j_{dark}	pA	Dark current.	8.2–21	13.24	(16,22,40,47,48,70,72,88–94)
j_{cG}^{max}	pA	Maximum cGMP-gated channel current.		3550	
j_{ex}^{sat}	pA	Saturated exchanger current.	1–2	1.8	(95–97)
k_{cat}/K_m	$\mu M^{-1}\ s^{-1}$	Hydrolytic efficiency of activated PDE dimer.	450–820	540	(17,54,98)
$k_{\sigma;hyd}$	$\mu m^3\ s^{-1}$	Surface hydrolysis rate of cGMP by dark-activated PDE.		2.8×10^{-5}	
$k^*_{\sigma;hyd}$	$\mu m^3\ s^{-1}$	Surface hydrolysis rate of cGMP by light-activated PDE.	0.75–1.37	0.9	
k_E	s^{-1}	Rate constant for inactivation of PDE.	5–11.5	6	(23,31,47,99)
k_R	s^{-1}	Rate constant for inactivation of Rh.	1.4–11	8.5	(47,61)
k_{T^*E}	$\mu m^2\ s^{-1}$	Kinetic constant describing the formation of T*·E complex and thus the production of E*.	1	1	(9)
K_{cyc}	nM	Half-saturating $[Ca^{2+}]$ for GC activity.	73–400	129	(31,47,70,71)
K_{cG}	μM	[cGMP] for half-maximum cGMP-gated channel opening.		20	(16)
K_{ex}	μM	$[Ca^{2+}]$ for half-maximum exchanger channel opening.	0.9–1.6	1.6	(16,96)
l_b	μm	Width of the incisure.		0.2593	(56)
l_r	μm	Length of the incisure.		0.2828	(56)
ν	—	Ratio between interdiscal space and disk thickness.	0.56–1	1	(16,17,54,57)
$\nu\varepsilon$	nm	Interdiscal space.		14.5	(17,57,86,87)
ν_{RE}	s^{-1}	Rate of PDE formation per fully activated Rh.	120–220	170	(16,46,49,54)
ν_{RG}	s^{-1}	Rate of transducin formation per fully activated Rh.	120–220	170	(16,46,49,54)
n	#	Number of disks.		814	
n_{inc}	#	Number of incisures.	1	1	(17,56,57)
N_{Av}	$\#mol^{-1}$	Avogadro number.	6.02×10^{23}	6.02×10^{23}	
m_{cyc}	—	Hill coefficient for GC effect.	2.3–4	2.45	(31,47,70–72)
m_{cG}	—	Hill coefficient for cGMP-gated channel.	3	3	(17,47,71,72,92)
$[PDE]_\sigma$	$\#\mu m^{-2}$	Surface density of dark-activated PDE.	500–1000	750	(16,17,83,86,100)
R	μm	Radius of disk.	0.45–1	0.7	(16,17,57,68,83,86,87,101)
σ	—	Ratio between outer shell thickness and disk thickness.		15:14.5	
$\sigma\epsilon$	nm	Distance between the disk rim and the plasma membrane (outer shell thickness).	15	15	(17,59)
Σ_{rod}	μm^2	Lateral surface area of ROS.		103.8	
V_{cyt}	μm^3	Cytoplasmic volume.		18.16	

adjusting the value of ν_{RE}. The calibration is minimal, and the parameters always remain within the published range of ν_{RE} ($120 \sim 220\ s^{-1}$ (16,46,49,54). These adjustments have little or no effect on the CV of E*, and response current I(t) for the following reasons:

1. All the remaining parameters have been kept unchanged; and
2. The adjustments of ν_{RE} amount to an equal multiplication factor to each of the ν_j.

The latter has no effect on the CV of E**, in view of the explicit formula (Eq. 15).

VARIABILITY OF E*

Table 1 reports the CV for the scalar quantities E**, t^*_{peak}, and E*(t^*_{peak}) defined in Eq. 12 for each of the cases indicated in Random Events Contributing to SPR Variability, and for an Rh* shutoff mechanism occurring in $n = 2, 3, 4, 5$ steps. The first result is that for Cases 1 and 2, the CV of any of these

TABLE 4 Parameters for the Salamander ROS

Symbol	Units	Definition	Range	Value	References
α_{max}	$\mu M\ s^{-1}$	Maximum rate of cGMP synthesis at low Ca^{2+} concentration.	40–50	50	(16,49)
$\alpha_{min}/\alpha_{max}$	—	Ratio of α_{min} to α_{max}.	0.00–0.02	0.02	(16,49)
A_{inc}	μm^2	Area of the incisure.	0.82	0.8	(55)
β_{dark}	s^{-1}	Rate of cGMP hydrolysis by dark-activated PDE.	1	1	(14–16,49)
B_{cG}	—	Buffering power of cytoplasm for cGMP.	1–2	1	(16,17,49)
B_{Ca}	—	Buffering power of cytoplasm for Ca^{2+}.	10–50	20	(16,49,61)
c_{GE}	—	Coupling coefficient from G* to E*.	<1	1	(16,54)
$[cGMP]_{dark}$	μM	Concentration of cGMP in the dark.	2–4	3.0046	(49,62)
$[Ca^{2+}]_{dark}$	nM	Concentration of Ca^{2+} in the dark.	400–700	653.7	(49,62)
D_{cG}	$\mu m^2\ s^{-1}$	Diffusion coefficient for cGMP.	50–196	160	(14,55,63)
D_{Ca}	$\mu m^2\ s^{-1}$	Diffusion coefficient for Ca^{2+}.	15	15	(64)
D_{E^*}	$\mu m^2\ s^{-1}$	Diffusion coefficient for activated PDE.	0.8	0.8	(17)
D_{G^*}	$\mu m^2\ s^{-1}$	Diffusion coefficient for activated G protein.	1.5	1.5	(17)
D_{R^*}	$\mu m^2\ s^{-1}$	Diffusion coefficient for activated Rh.	0.7	0.7	(17)
ε	nm	Disk thickness.	10–14	14	(16,62)
η	nm	Volume/surface ratio.		7	
$\mathcal{F}$	$\mathcal{C}mol^{-1}$	Faraday's constant.	96,500	96,500	(16,49)
f_{Ca}	—	Fraction of cGMP-activated current carried by Ca^{2+}.	0.1–0.2	0.17	(16,49)
H	μm	Height of ROS.	20–28	22.4	(16,62)
j_{dark}	pA	Dark current.	74	65.862	(16)
j_{cG}^{max}	pA	Maximum cGMP-gated channel current.	70–7000	7000	(49)
j_{ex}^{sat}	pA	Saturated exchanger current.	17–20	17	(16)
k_{cat}/K_m	$\mu M^{-1}\ s^{-1}$	Hydrolytic efficiency of activated PDE dimer.	340–600	400	(17,49,54)
$k_{\sigma;hyd}$	$\mu m^3\ s^{-1}$	Surface hydrolysis rate of cGMP by dark-activated PDE.	—	7×10^{-5}	(14)
$k^*_{\sigma;hyd}$	$\mu m^3\ s^{-1}$	Surface hydrolysis rate of cGMP by light-activated PDE.	—	1	(13,14)
k_E	s^{-1}	Rate constant for inactivation of PDE.	0.58–0.76	0.6	(61)
k_R	s^{-1}	Rate constant for inactivation of Rh.	1.69–3.48	2.5	(61)
k_{T^*E}	$\mu m^2\ s^{-1}$	Kinetic constant describing the formation of T*·E complex and thus the production of E*.	1	1	(9)
K_{cyc}	nM	Half-saturating $[Ca^{2+}]$ for GC activity.	100–230	135	(49,62)
K_{cG}	μM	[cGMP] for half-maximum cGMP-gated channel opening.	13–32	20	(16,49,62)
K_{ex}	μM	$[Ca^{2+}]$ for half-maximum exchanger channel opening.	1.5; 1.6	1.5	(49,62)
l_b	nm	Width of the incisure.	10–12	15	(55)
l_r	μm	Length of the incisure.		4.6377	(15)
ν	—	Ratio between interdiscal space and disk thickness.		1	
$\nu\varepsilon$	nm	Interdiscal space.	10–14	14	(16,62)
ν_{RE}	s^{-1}	Rate of PDE formation per fully activated Rh.	120–220	195	(16,46,49,54)
ν_{RG}	s^{-1}	Rate of transducin formation per fully activated Rh.	120–220	195	(16,46,49,54)
n	#	Number of disks.	1000	800	(49,62)
n_{inc}	#	Number of incisures.	15–30	23	(55,65–69)
N_{Av}	$\#mol^{-1}$	Avogadro number.	6.02×10^{23}	6.02×10^{23}	
m_{cyc}	—	Hill coefficient for GC effect.	2	2	(16,54,63)
m_{cG}	—	Hill coefficient for cGMP-gated channel.	2–3	2.5	(16)
$[PDE]_\sigma$	$\#\mu m^{-2}$	Surface density of dark-activated PDE.	100	100	(16)
R	μm	Radius of disk.	5.5	5.5	(49,62)
σ	—	Ratio between outer shell thickness and disk thickness.		15:14	(49,62)
$\sigma\varepsilon$	nm	Distance between the disk rim and the plasma membrane (outer shell thickness).	15	15	(49,62)
Σ_{rod}	μm^2	Lateral surface area of ROS.		773.5	(62)
V_{cyt}	μm^3	Cytoplasmic volume.	1000	1076	(16,62)

quantities is essentially zero. Thus, neither the randomness of the activation site nor the random walk of Rh* contribute to the CV of E*. For the mouse, the presence or absence of incisures does not affect the CV of E*. For the salamander, the presence of incisures tends to slightly reduce the CV of E*. The reduction is ~1%. This effect is most likely due to the different geometry of the ROS for mouse and salamander. Mice have long and thin ROS with one incisure, exposing only a modest area. The complement of the incisure is essentially the whole disk. Salamander ROS have a large cross section bearing up to 30 incisures, exposing a relatively large area. We believe that their number, more than the area they expose, is responsible for a slightly reduced CV; indeed, they tend to create essentially equal compartments, and rhodopsin activated by a photon captured in one of them tends to remain there, thereby yielding a more reproducible response.

The multistep deactivation mechanism of Rh* seems to be responsible for the CV of E*. Moreover the CV produced by

Case 3, to which only the randomness of the shutoff mechanism contributes, seems to be roughly the same as that of Case 4, where all components are allowed to be random. In all cases, CV decreases with increasing n. For the biochemical choice of the NN mechanism, the largest CV drop occurs when the number of steps to shutoff goes from 2 to 3. As the number of inactivation steps further increases to 4 and 5, the CV remains essentially the same.

Instead, for the theoretical choice of EE, an increase in the number of shutoff steps from 3 to 5 yields a decrease of CV by up to 12%. For the case EE, the theoretical formula (Eq. 15) predicts a CV for E** of $1/\sqrt{n}$, irrespective of the values of the parameters. Accordingly, the simulated CV for E** reported in Table 1 is exactly $1/\sqrt{n}$ both for mouse and salamander, within possible relative statistical errors $<1\%$.

The comparison of the CV of E**, E*(t^*_{peak}), and t^*_{peak} for the biochemically motivated case NN and the theoretical case EE demonstrates that when the number n of Rh* shutoff steps increases, the latter produces a more stable process. For $n = 2$, the CV of these quantities is essentially the same for the NN and EE cases. Since n increases to 3,4,5, it is higher for NN than for EE by up to 35%, for $n = 4, 5$. Thus, the EE biochemistry produces a process more stable than the realistic biochemistry NN—most likely because of a more regular distribution of times τ_j and because the catalytic constants ν_j are all equal to ν_{RE}.

In Fig. 3, *A* and *C*, and Fig. 4, *A* and *C*, we report the graphs of the CV for E**(t) as functions of time only for Case 4. Indeed, this is the biologically realistic case, where all the parts of the phenomenon are permitted to be random. This variability functional is defined in Eq. 12.

In all cases, the CV decreases with increasing n. For the case of the biochemistry NN, there is a drop in CV in going from two shutoff steps of Rh* to $n = 3$. For mechanisms with a number of phosphorylations $n \geq 3$, the CV of E**(t) is essentially indistinguishable for $n = 3, 4, 5$. Within the timecourse of the phenomenon ($\approx$1.8 s for the salamander and $\approx$0.5 s for the mouse), the CV of E**(t) does not exceed 0.5, at least for $n \geq 3$, and as $t \to \infty$, it tends asymptotically to $\approx$0.6.

For the theoretical biochemistry EE, the decrease of CV for n going from 2 to 3, 4, and 5 is more dramatic, although from 4 to 5 the drop in CV is approximately half of that for the preceding values of n. Within the timecourse of the phenomenon, the CV of E**(t), for Rh* shutting off in either 4 or 5 steps, does not exceed 0.4—and as $t \to \infty$, it tends asymptotically to $\approx$0.42, even for $n = 4, 5$.

In all cases, despite the different geometry of the disks, including the different distribution of incisures, the CV of E**(t) for mouse and salamander are comparable.

VARIABILITY OF THE PHOTOCURRENT

In Table 2 we have reported the CV of the scalar quantities I**, I(t_{peak}), and t_{peak}, defined in Eq. 13 for each of the Cases 3 and 4 indicated in Random Events Contributing to SPR Variability, and for an Rh* shutoff mechanism occurring in $n = 2, 3, 4, 5$ steps. We do not report the simulations for Cases 1 and 2 that record the random effects of the activation site and the random walk of Rh*. As shown in Table 1, these effects have a negligible effect of the CV of I**, I(t_{peak}), and t_{peak}. These random components, which have a negligible effect by themselves, affect the system more noticeably when coupled with the random shutoff of Rh*. This becomes apparent by comparing the Case 3 (randomness only due to shutoff mechanism) and Case 4 (all components are allowed to be random; see Table 2). The results exhibit a pattern similar to those in Table 1, although at considerably lower values of CV.

The biochemistry of NN

In all cases, there is a drop in CV of 10–15% in going from $n = 2$ to $n = 3$, and then for $n = 3, 4, 5$ the CV tends to remain virtually constant. This suggests that an increase in the number of steps in the shutoff process of Rh* to >3–4 steps does not significantly decrease the CV of these functionals, which remain within 2–3% of each other. For the salamander, the presence of incisures increases the CV of I** by 8–13%, and the CV of I(t_{peak}) by 2–10%. However, the CV of t_{peak} decreases slightly (by $\leq$5%). Thus, in terms of photocurrent the presence of incisures in the salamander ROS tends to generate a less stable system and in terms of peak time a slightly more stable system. This is likely explained by more efficient and rapid diffusion of cGMP afforded by the vertical shafts created by the incisures. The effects of incisures in the mouse are similar with reduced quantitative impact, except that in the presence of incisures, the CV of t_{peak} also increases.

The biochemistry EE

The results for the theoretical case EE are similar, except that the CV of the various functionals decrease as n increases, although at a decreasing rate for increasing n. The pattern suggest an asymptotic limit as $n \to \infty$ for these CV. It is worth noting that for the mouse, the CV of I(t_{peak}) for $n = 5$ is smaller than the experimental values reported in the literature (6,8,10,58). This suggests that even assuming the biochemistry EE, the number of steps to Rh* to quenching is limited. It also suggests that the analysis of the CV of the SPR cannot be based only on the number n of steps postulated to shutoff of Rh*; rather, it would require a stipulation on the nature of these steps, which we have translated in the structure of the sequences $\{\nu_j\}$ and $\{\tau_j\}$.

Lumped models

Table 2 contains two extra sets of simulations labeled by the transversally well-stirred (TWS) model and the globally well-stirred (GWS) model, as opposed to the space-resolved (SR) model. The latter corresponds to the model we are using in these simulations, originating from homogenization and concentrated capacity, as described in the literature

(13,15,29,30). The TWS model lumps all quantities in the ROS along its longitudinal axis, and takes into account only the diffusion of the second messengers cGMP and Ca^{2+} along this axis. The GWS model lumps together all quantities as each satisfying global first-order reactions, devoid of any spatial characteristics, such as geometry, diffusion in interdiscal spaces, etc.

In the literature (13,15) we have described how to obtain the GWS model from the SR model, and how to simulate with them and compare the outputs. The main reason we report the results of these simulations is that the GWS model is the most commonly used (16,49) because of its mathematical and computational simplicity, and the TWS model is sometimes used as the first attempt to take into account the spatiotemporal features of the system (53,59).

For the salamander, for the biochemistry NN, there is a relative difference of $\geq$10% between the CV calculated with the SR model and the TWS model. That difference increases to 20–40% in going from the SR to the GWS model. Discrepancies of the same order or larger occur for the theoretical biochemistry EE (Table 2). In all cases, the CV computed with the coarser models TWS and GWS is larger, and it increases with the coarseness of the model. In particular, the more the model is well stirred, the larger is the CV. Thus, lumped models yield a variability larger than what is physically expected, due to the damping effects of the diffusion process. The latter are being detected and factored in by our the SR model.

The CV of the photocurrent over the timecourse of the response

Fig. 3, *B* and *D*, and Fig. 4, *B* and *D*, report the CV of the total relative charge produced up to time t, for the physically realistic Case 4, where all random components are present. In all cases, CV decreases with increasing n. However, for the biochemistry NN, the CV stabilizes for $n \geq 3$ and it is essentially the same for $n = 3, 4, 5$. For the theoretical EE case, the CV keeps decreasing with increasing n, although at a decreasing rate for increasing n, and points to some theoretical asymptotic behavior as $n \rightarrow \infty$. Fig. 5 compares the CV of the total

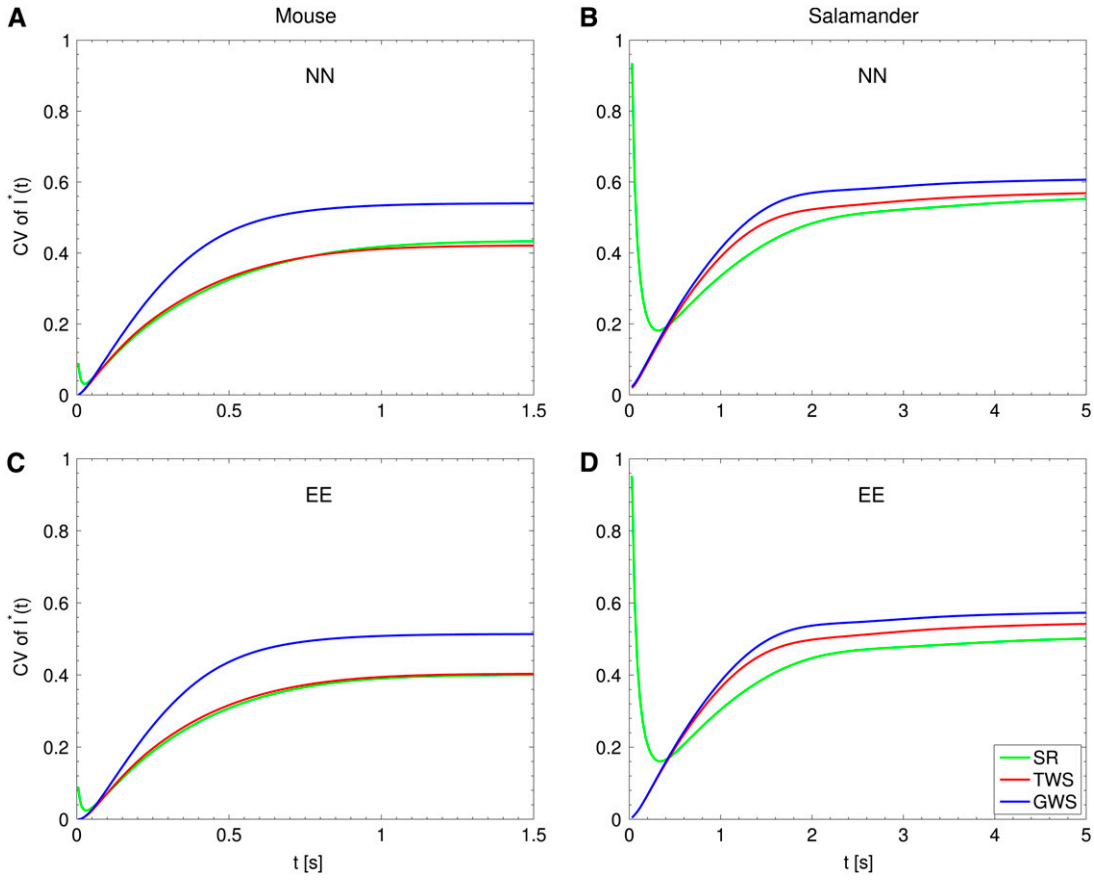

FIGURE 5 CV of $I^*(t) = \int_0^t I(s)ds$: total relative charge up to time t. (*SR*) Space-resolved; (*TWS*) transversally well-stirred; (*GWS*) globally well-stirred; (*NN*) shutoff of Rh* in n biochemical states of decreasing duration and catalytic activity (see Biochemical Sequences $\{\tau_j\}$ and $\{\nu_j\}$); and (*EE*) shutoff of Rh* in n theoretical states of equal duration and equal catalytic activity (see Sequence for Which $\tau_j\nu_j = \text{Const}$). All simulations assume all activation steps as random (Case 4 of Random Events Contributing to SPR Variability). In all cases, the CV computed with the GWS model is higher than the one computed with the other two models. A high CV at early times for the salamander, detected by the SR model (where geometry and incisures matter), is not detected by the lumped models TWS and GWS. This suggests the interpretation that a high CV at the inception of the activation cascade is due to the architecture of the salamander ROS.

relative charge up to time t computed with the SR model to the CV of the same quantity computed by the TWS and GWS models. In all cases, the CV computed with the GWS model is higher than the one computed with the other two models.

A peculiar, apparently reverse effect, can be observed for the salamander, at early times. The CV is initially large and then rapidly drops. This effect seems to be due to the random position of the activation site. Indeed, photons absorbed close to the disk boundary yield a faster response than those absorbed far away from the boundary, say near the center of the disk. After a short time, depending on the diffusivity coefficients on the disk and on the disk radius, this difference is reduced. In the mouse, where diffusivities are larger and the radius is smaller than similar parameters in the salamander, no significant increase of variability at early times is observed.

DISCUSSION

Rods are highly polarized, and intricately organized, neuronal cells, with elaborate outer segment structure. There is a precise geometry of stacked disks in the cytoplasm, with elaborate precisely aligned incisures that serve to facilitate the longitudinal diffusion of second messengers (15). Rod disks house the integral membrane and peripheral membrane proteins that perform photon capture and chemical amplification of the visual signal. Perturbations of this complex cellular architecture lead to retinal degeneration by triggering apoptosis (60).

We recently introduced a mathematical model of the dynamics of visual transduction that incorporates the precise geometry of outer segments. To make this phenomenon computationally tractable, the model reduced the complex geometry of the outer segment to a simpler one by separating the two-dimensional diffusion of molecules on disks and plasma membrane from the three-dimensional cytoplasmic diffusion. Using this model, we were able to capture fine spatial and temporal dynamics of visual transduction. The computational implementation of the model has allowed us to reproduce the local effects that characterize rod signaling in response to light. This has provided a quantitative assessment of the notion of spread of excitation (13,14), and of the impact of the activation site on the single photon response. In particular, these studies showed that variation in single photon responses that were thought to be random, can be accounted for to some degree, by the distance of the site at which the photon hits from the plasma membrane.

Recently we took advantage of the capabilities of this model to study the role of incisures, intricate structures that are held together with bivalent proteins called peripherin/retinal degeneration-slow, or (rds). Our modeling showed that incisures allowing for larger cytoplasmic spaces, favor the longitudinal diffusion of cGMP and Ca. This effect leads to larger light-responses, and depends on the number of incisures and their geometry.

In this work we investigated the issue of variability and addressed one of the long-standing challenges in the field, the unexpectedly high reproducibility of a single photon response. It has been established that despite the stochastic nature of each step in the visual transduction cascade, the single photon response is more reproducible than would be expected based on the variability introduced at each step of the cascade.

There are several random events that contribute to the variability of the single photon response. These include the random activation site, the random path of Rh*, and the random shutoff mechanism. Biochemical studies of the shutoff mechanism provide constraints for the modeling. Rhodopsin quenching occurs through rhodopsin kinase phosphorylation on no more than six serine and threonine residues (in the mouse), and the catalytic activity of rhodopsin kinase is greatest when no phosphorylations have occurred (more available targets on the substrate). It was shown experimentally that the first 2–3 phosphorylations account for much of the turnoff (40).

The main objective of this study was to understand how such an inherently random process ultimately yields highly reproducible responses. Our model allows us to query the relative impact of the randomness at each step of response variability. We found that variation of the activation site contributes only at early times to the CV of the photoresponse, whereas the random path of Rh* has a negligible effect at all times. The major source of variability is the randomness of the turnoff mechanism.

Reproducibility of the single photon response is experimentally measured at the final output of photocurrent, whereas randomness occurs at the level of the activation cascade. One of the objectives of our study was to separate these two modules. Because the model includes a full spatiotemporal description of the development of the response within rod geometry, it can separately evaluate the contribution of the activation and turnoff of the cascade taking place at the disk membrane and the diffusion of second messengers in the cytoplasm. The activation and turnoff are rather variable events, as expected (see Variability of E*), whereas the resulting photocurrent has a dramatically reduced CV due to the stabilizing effects of the diffusion of the second messengers in the cytoplasm. This is a novel and rather unexpected result.

In previous studies, the random shutoff mechanism of Rh*, and its random lifetime $\boldsymbol{t}_{\mathrm{Rh}^*}$, were suggested as the cause of reduced variability (6–8,46). The data of Rieke and Baylor (6) were interpreted by postulating that t_{Rh^*} itself has a low variability. The statistical analysis of Rieke and Baylor (6) yields a sample of cumulative lifetimes t_{Rh^*} with CV of ~20%, which is of the same order as the CV of the peak current amplitudes. Thus, a low variability of the peak amplitude was postulated to be the result of a low variability of the active lifetime t_{Rh^*}. Essentially the same data were interpreted by Whitlock and Lamb (8) by advancing the hypothesis that shutoff of Rh* occurs abruptly and by fitting the data by a single parameter t_{Rh^*}. Their analysis, while reproducing a CV of ~20% for the peak current, estimates the CV of t_{Rh^*} as ~40% (8,10). Thus postulating abrupt shutoff of Rh* seems to indicate that the system remains stable,

despite larger variations of t_{Rh^*}. Calcium feedback mechanisms do not seem to have any significant regulatory effect on the variability of t_{Rh^*}. Experiments with clamped calcium, while yielding slower responses with greater peak amplitudes, exhibit the same CV of ~20% for both the time-to-peak, and the peak currents (6,8). Our numerical simulations with clamped calcium reproduce this behavior (data not shown).

The numerical simulations of Ramanathan et al. (9), after a single isomerization show that the activated transducin T* remains essentially confined in a circular spot about the activation site. Such localization was proposed as a possible mechanism of variability suppression. That is, random instances where the lifetime of Rh* greatly exceeds its mean value, do not correspond to a prolonged increase in [PDE*], and therefore in electrical response. In the simulations of Ramanathan et al. (9), Rh* is kept fixed, the dynamics of E* is neglected, and variability is measured at peak T*. For these reasons, the results of Ramanathan et al. (9) are not directly comparable to the others (6,8,28).

Our numerical simulations show that in the salamander, for t_{Rh^*} ranging up to 4, i.e., a time-interval tenfold-larger than rhodopsin average lifetime t_{Rh^*}, no saturation of [PDE*] occurs. Similarly for the mouse, for t_{Rh^*} ranging up to 0.5 (a time-interval approximately threefold-larger than t_{Rh^*}), no saturation of [PDE*] occurs. We have observed that the spot formation predicted by Ramanathan et al. (9) does actually occur, but at times >4.5 s for the salamander, and 0.5 s for mouse. These times are considerably larger than the time-course of the SPR. The parameters we use in our simulations are those in Tables 3 and 4. We are uncertain of the parameters in Ramanathan et al. (9).

Thus, a summary of the current working hypotheses in the field is that either the active lifetime t_{Rh^*} has low variability, or the final output response is relatively insensitive to variations of t_{Rh^*}.

Our analysis shows that the random shutoff mechanism of Rh* and its lifetime t_{Rh^*} are the source of variability, whereas its reduction depends on another mechanism, downstream from the activation cascade, which is the smoothing effect of second messenger diffusion.

Postulating a theoretical increase in the number of biochemical events leading to Rh* quenching yields a theoretical reduction of the variability of E*. However, it is biochemically unrealistic to increase the number of biochemical events in rhodopsin shutoff to greater than seven steps, because there are only six phosphorylation sites on mouse rhodopsin, and arrestin binding occurs fully after three phosphates are attached to rhodopsin (18). Likewise, the mean times of permanence of Rh* in its phosphorylated states cannot obligingly grow longer to keep the functional contribution of these steps comparable if the known biochemistry is taken into account (see Statistics and Biochemistry). In short, the sequences $\{\tau_j\}$ and $\{\nu_j\}$ are constrained by biochemical and mathematical limitations (See the sections on Biochemical sequence, $\{\tau_j\}$ and $\{\nu_j\}$, and More on statistics and biochemistry). Enforcing the experimentally known information on these sequences along with their mathematical compatibility has the net result of providing further evidence that only unphosphorylated and the first few phosphorylated states of Rh* are responsible for the bulk of the SPR.

Thus, the variability must be limited by some other mechanism. We have established that the diffusion of the second messengers in the cytoplasm is one such stabilizing mechanism. This is accomplished by an extensive set of simulations on a mathematical model which has the capability of separating the process into functional modules (activation, transduction, etc.) and into physical geometrical modules (size, shape, incisures, etc.). To stress the relevance of these components, our analysis has been conducted on both mouse and salamander, in view of their anatomical difference.

Diffusion versus diffusivity

We have performed numerical simulations on the system given in Appendix A, where D_{cG} and D_{Ca} have been increased two- or threefold. The simulations show that the resulting CV is larger. Greater increases of D_{cG} and D_{Ca} further increase the CV. As could be expected, the CV of the well-stirred model seems to be the asymptotic limit of the CV generated by progressive increase of diffusivities of cGMP and Ca^{2+}. We have also performed numerical simulations on the same system in Appendix A, where D_{cG} and D_{Ca} have been decreased two- and threefold. The numerical simulations show that the corresponding CV decreases, thereby providing further evidence that CV increases with D_{cG} and D_{Ca}. Thus the geometry of the rod stabilizes the process by limiting the rate of diffusion of the second messengers. As $D_{cG}, D_{Ca} \to \infty$, then the spatiotemporal system in Appendix A asymptotically approaches the well-stirred model where [cGMP] and [Ca^{2+}] are constant in space and depend only on time. Thus, instant by instant, as D_{cG} and D_{Ca} increase, the concentrations tend to equalize at infinite speed, thereby neglecting the hindrance of the layered geometry and leading to the well-stirred model. The system, devoid of space dynamics, passes along the variability of the activated effector E*, to the variability of the relative current drop. Conversely, in the fully resolved model, the second messenger cGMP is forced to move through the layered geometry of the ROS before causing a current suppression. In this process, the differences between the amount of cGMP hydrolyzed in response to the activation of a single Rh* become smoothed out, making the electrical response at the plasma membranes less variable. As an analogy, consider a container filled with fluid at constant space concentration, although that can vary in time. Consider now an ideal box immersed in the fluid; ''ideal'' means that the fluid goes freely with no hindrance through its boundary and its interior. Such a box will record the same concentration and the same time fluctuations of the concentration of the bath. By contrast, a box made out of tiny interconnected compartments would oppose penetration, and

for any finite time would exhibit density fluctuations smaller than those of the bath. In summary, the more spatially uniform the process is, the more efficiently the variability of E* is passed along to the current suppression. For example, the incisures that tend to generate more uniform spatial concentrations of cGMP and Ca^{2+} also increase the CV.

Concluding remarks

The geometry of rod outer segments is conserved in all vertebrates, and its disorganization causes the death of photoreceptor cells. Clearly, this geometry and the spatiotemporal aspects of signal propagation are important contributors to SPR and have to be taken into account when attempting to model the process. Models that treat the rod outer segment as homogeneous or well stirred are not able to separate, and effectively examine, the roles of the activation and turnoff that occur on the two-dimensional disk surface and three-dimensional diffusion of second messengers. Our spatiotemporal modeling approach makes this feasible. Our results clearly show that the high reproducibility of a SPR can be explained without invoking biochemically unrealistic increases in the number of turnoff steps. Our model reveals that the damping effect of second-messenger diffusion makes the current output much more reproducible than the light activation of PDE. Cones, as well as invertebrate photoreceptors, have very different geometry. Our model will also be useful to examine the functional implications of those geometries.

APPENDIX A: DYNAMICS OF THE CASCADE

TABLE 5 Symbol key

Symbol	Definition
H	Height of the ROS.
R	Radius of the disks inside the ROS (disregarding incisures).
D_R	Disk of radius R centered at the origin of $\mathcal{R}^2$.
m	Number of incisures.
$\mathcal{V}_j$	Limiting j^{th} incisures, assimilated to segments of length $R - r_{o,j}$.
r_j	Radial variable on $\mathcal{V}_j$ with origin at $r_{o,j}$.
$\theta_{\varepsilon_o,j}(r_j)$	Geometry of the j^{th} incisure with tip at $r_{o,j}$.
D_{eff}	$D_R - \cup_{j=1}^{m}\mathcal{V}_j$ effective domain of the activation cascade.
k	Number of distinct activated disks each by a single photon.
$D^*_{i,\,eff}$	i^{th} activated disk.
Ω	$D_R \times (0, H)$ limiting cylinder enclosing the stack of disks D_R.
Ω_{eff}	$D_{eff} \times (0, H)$ limiting domain available for diffusion of cGMP and Ca^{2+}.
$\mathcal{B}_j$	$\mathcal{V}_j \times (0, H)$ limiting vertical rectangles cut on the limiting ROS by the limiting incisures aligned in series.
S	Limiting outer shell (same as lateral boundary of Ω).
$d\eta$	Surface measure on S.
ε_o	Width of each disk.
$\nu\varepsilon_o$	Width of each interdiscal space.
$\sigma\varepsilon_o$	Width of the outer shell.
$1 - \mu_o$	Volume ratio of cytosol to the volume of the ROS.
[cGMP]	[cGMP] in the interior of the limiting ROS.
$[cGMP]_*$	[cGMP] in the activated disk(s).
$[cGMP]_S$	[cGMP] in the limiting outer shell.
$[cGMP]_{\mathcal{B}j}$	[cGMP] on $\mathcal{B}_j$.
$[Ca^{2+}]$	$[Ca^{2+}]$ in the interior of the limiting ROS.
$[Ca^{2+}]_*$	$[Ca^{2+}]$ in the activated disk(s).
$[Ca^{2+}]_S$	$[Ca^{2+}]$ in the limiting outer shell.
$[Ca^{2+}]_{\mathcal{B}j}$	$[Ca^{2+}]$ on $\mathcal{B}_j$.
∇_S	Gradient along the cylindrical variables of S.
$\nabla_{\mathcal{B}_j}$	Gradient along the (r_j, z) variables of $\mathcal{B}_j$.
$\nabla_{(x,\,y)}$	Gradient along the horizontal variables (x, y).

Weak formulation of the dynamics of cGMP

$$
\begin{aligned}
&(1-\mu_o)\Bigg\{\int\int\int_{\Omega_{eff}}[cGMP](t)\varphi(t)dxdydz\\
&\quad-\int\int\int_{\Omega_{eff}}[cGMP]_{dark}\varphi(0)dxdydz\\
&\quad+\int_0^t\int\int\int_{\Omega_{eff}}\{-[cGMP]\varphi_t+D_{cG}\nabla_{(x,y)}[cGMP]\cdot\nabla_{(x,y)}\varphi\\
&\quad-[\alpha([Ca^{2+}])-\beta_{dark}[cGMP]]\varphi\}dxdydz\,d\tau\Bigg\}_{interior}\\
&+\nu\varepsilon_o\Bigg\{\sum_{i=1}^{k}\int\int_{D^*_{i,eff}}\{[cGMP]_*(t)\varphi(t)-[cGMP]_{dark}\varphi(0)\}dxdy\\
&\quad+\sum_{i=1}^{k}\int_0^t\int\int_{D^*_{i,eff}}\Bigg\{-[cGMP]_*\varphi_t+D_{cG}\nabla_{(x,y)}[cGMP]_*\cdot\nabla_{(x,y)}\varphi\\
&\quad-\Bigg(\alpha([Ca^{2+}]_*)-\beta_{dark}[cGMP]_*\\
&\quad-\frac{k^*_{\sigma;hyd}}{\nu\varepsilon_o}[PDE^*]_\sigma[cGMP]_*\Bigg)\varphi\Bigg\}dxdyd\tau\Bigg\}_{activated\ discs}\\
&+\sigma\varepsilon_o\Bigg\{\int\int_S\{[cGMP]_S(t)\varphi(t)-[cGMP]_{dark}\varphi(0)\}dS\\
&\quad+\int_0^t\int\int_S\{-[cGMP]_S\varphi_t+D_{cG}\nabla_S[cGMP]_S\cdot\nabla_S\varphi\}dSd\tau\Bigg\}_{outer\ shell}\\
&+2\Bigg\{\sum_{j=1}^{m}\int\int_{\mathcal{B}_j}r_j\theta_{j,\varepsilon_o}(r_j)\{[cGMP]_{\mathcal{B}_j}(t)\varphi(t)dr_jdz\\
&\quad-[cGMP]_{dark}\varphi(0)\}dr_jdz\\
&\quad+\sum_{j=1}^{m}\int_0^t\int\int_{\mathcal{B}_j}r_j\theta_{j,\varepsilon_o}(r_j)\{-[cGMP]_{\mathcal{B}_j}\varphi_t\\
&\quad+D_{cG}\nabla_{\mathcal{B}_j}[cGMP]_{\mathcal{B}_j}\cdot\nabla_{\mathcal{B}_j}\varphi\}dr_jdzd\tau\Bigg\}_{incisures}=0,
\end{aligned}
$$

for all $t > 0$ and all smooth, real valued functions φ in $\bar{\Omega}\times\mathcal{R}^+$. Here

$$\alpha([\mathrm{Ca}^{2+}]) = \alpha_{\min} + (\alpha_{\max} - \alpha_{\min})\frac{K_{\mathrm{cyc}}^{m_{\mathrm{cyc}}}}{K_{\mathrm{cyc}}^{m_{\mathrm{cyc}}} + [\mathrm{Ca}^{2+}]^{m_{\mathrm{cyc}}}}$$

$$\alpha([\mathrm{Ca}^{2+}]_*) = \alpha_{\min} + (\alpha_{\max} - \alpha_{\min})\frac{K_{\mathrm{cyc}}^{m_{\mathrm{cyc}}}}{K_{\mathrm{cyc}}^{m_{\mathrm{cyc}}} + [\mathrm{Ca}^{2+}]_*^{m_{\mathrm{cyc}}}}$$

$$\text{where} \quad \alpha_{\max} = k_{\mathrm{GC,max}}[\mathrm{GC}], \quad \alpha_{\min} = k_{\mathrm{GC,min}}[\mathrm{GC}].$$

Here $k_{\mathrm{GC,min}}$ and $k_{\mathrm{GC,max}}$ are the minimum and maximum catalytic rates of production of cGMP by guanylyl cyclase GC occurring, respectively, as $[Ca^{2+}] \to \infty$ and as $[Ca^{2+}] \to 0$.

Weak formulation of the dynamics of Ca^{2+}

$$\begin{aligned}
&(1-\mu_{\mathrm{o}})\Bigg\{\int\int\int_{\Omega_{\mathrm{eff}}}\{[\mathrm{Ca}^{2+}](t)\varphi(t) - [\mathrm{Ca}^{2+}]_{\mathrm{dark}}\varphi(0)\}dxdydz \\
&\quad + \int_0^t\int\int\int_{\Omega_{\mathrm{eff}}}\{-[\mathrm{Ca}^{2+}]\varphi_{\mathrm{t}} \\
&\quad + D_{\mathrm{Ca}}\nabla_{(\mathrm{x,y})}[\mathrm{Ca}^{2+}]\cdot\nabla_{(\mathrm{x,y})}\varphi\}dxdydz\,d\tau\Bigg\}_{\mathrm{interior}} \\
&+\nu\varepsilon_{\mathrm{o}}\Bigg\{\sum_{\mathrm{i}=1}^{\mathrm{k}}\int\int_{\mathrm{D}^*_{\mathrm{i,eff}}}\{[\mathrm{Ca}^{2+}]_*(t)\varphi(t) - [\mathrm{Ca}^{2+}]_{\mathrm{dark}}\varphi(0)\}dxdy \\
&\quad + \sum_{\mathrm{i}=1}^{\mathrm{k}}\int_0^t\int\int_{\mathrm{D}^*_{\mathrm{i,eff}}}\{-[\mathrm{Ca}^{2+}]_*\varphi_{\mathrm{t}} \\
&\quad + D_{\mathrm{Ca}}\nabla_{(\mathrm{x,y})}[\mathrm{Ca}^{2+}]_*\cdot\nabla_{(\mathrm{x,y})}\varphi\}dxdy\,d\tau\Bigg\}_{\substack{\mathrm{activated}\\ \mathrm{discs}}} \\
&+\sigma\varepsilon_{\mathrm{o}}\Bigg\{\int\int_{\mathrm{S}}\{[\mathrm{Ca}^{2+}]_{\mathrm{S}}(t)\varphi(t) - [\mathrm{Ca}^{2+}]_{\mathrm{dark}}\varphi(0)\}dS \\
&\quad + \int_0^t\int\int_{\mathrm{S}}\{-[\mathrm{Ca}^{2+}]_{\mathrm{S}}\varphi_{\mathrm{t}} + D_{\mathrm{Ca}}\nabla_{\mathrm{S}}[\mathrm{Ca}^{2+}]_{\mathrm{S}}\cdot\nabla_{\mathrm{S}}\varphi\}dS\,d\tau \\
&\quad + \int_0^t\int\int_{\mathrm{S}}\frac{1}{\sigma\varepsilon_{\mathrm{o}}B_{\mathrm{Ca}}\mathcal{F}}\Bigg\{\frac{j_{\mathrm{ex}}^{\mathrm{sat}}}{\Sigma_{\mathrm{rod}}}\frac{[\mathrm{Ca}^{2+}]_{\mathrm{S}}}{K_{\mathrm{ex}} + [\mathrm{Ca}^{2+}]_{\mathrm{S}}} \\
&\quad - \frac{1}{2}f_{\mathrm{Ca}}\frac{j_{\mathrm{cG}}^{\max}}{\Sigma_{\mathrm{rod}}}\frac{[\mathrm{cGMP}]_{\mathrm{S}}^{m_{\mathrm{cG}}}}{K_{\mathrm{cG}}^{m_{\mathrm{cG}}} + [\mathrm{cGMP}]_{\mathrm{S}}^{m_{\mathrm{cG}}}}\Bigg\}\varphi dS\,d\tau\Bigg\}_{\mathrm{outer\ shell}} \\
&+2\Bigg\{\sum_{\mathrm{j}=1}^{\mathrm{m}}\int\int_{\mathcal{B}_{\mathrm{j}}} r_{\mathrm{j}}\theta_{\mathrm{j},\varepsilon_{\mathrm{o}}}(r_{\mathrm{j}})\{[\mathrm{Ca}^{2+}]_{\mathcal{B}_{\mathrm{j}}}(t)\varphi(t) \\
&\quad - [\mathrm{Ca}^{2+}]_{\mathrm{dark}}\varphi(0)\}dr_{\mathrm{j}}dz \\
&\quad + \sum_{\mathrm{j}=1}^{\mathrm{m}}\int_0^t\int\int_{\mathcal{B}_{\mathrm{j}}} r_{\mathrm{j}}\theta_{\mathrm{j},\varepsilon_{\mathrm{o}}}(r_{\mathrm{j}})\{-[\mathrm{Ca}^{2+}]_{\mathcal{B}_{\mathrm{j}}}\varphi_{\mathrm{t}} \\
&\quad + D_{\mathrm{Ca}}\nabla_{\mathcal{B}_{\mathrm{j}}}[\mathrm{Ca}^{2+}]_{\mathcal{B}_{\mathrm{j}}}\cdot\nabla_{\mathcal{B}_{\mathrm{j}}}\varphi\}dr_{\mathrm{j}}dz\,d\tau\Bigg\}_{\mathrm{incisures}} = 0
\end{aligned}$$

for all $t > 0$ and all smooth, real valued functions φ in $\bar{\Omega}\times\mathcal{R}^+$.

Weak formulation of the dynamics of transducer and effector

$$\begin{aligned}
&\int\int_{\mathrm{D_{eff}}}[\mathrm{T}^*](t)\varphi(t)dxdy \\
&\quad + \int_0^t\int\int_{\mathrm{D_{eff}}}\{-[\mathrm{T}^*]\varphi_{\mathrm{t}} + D_{\mathrm{T}}\nabla[\mathrm{T}^*]\cdot\nabla\varphi\}dxdyd\tau \\
&= \int_0^t k_\ell\varphi(x(\tau),y(\tau)\tau)d\tau - \int_0^t\int\int_{\mathrm{D_{eff}}}k_{\mathrm{T^*E}}[\mathrm{E}][\mathrm{T}^*]\varphi dxdyd\tau \\
&\quad \int\int_{\mathrm{D_{eff}}}[\mathrm{E}^*](t)\varphi(t)dxdy \\
&\quad + \int_0^t\int\int_{\mathrm{D_{eff}}}\{-[\mathrm{E}^*]\varphi_{\mathrm{t}} + D_{\mathrm{E}}\nabla[\mathrm{E}^*]\cdot\nabla\varphi\}dxdyd\tau \\
&= \int_0^t\int\int_{\mathrm{D_{eff}}}\{k_{\mathrm{T^*E}}[\mathrm{E}][\mathrm{T}^*]\varphi - k_{\mathrm{E}^*}[\mathrm{E}^*]\varphi\}dxdyd\tau
\end{aligned}$$

for all $t > 0$ and all smooth, real valued functions φ in $\bar{D}_{\mathrm{R}}\times\mathcal{R}^+$.

APPENDIX B: COMPUTING THE VARIABILITY OF THE TOTAL NUMBER OF MOLECULES OF EFFECTOR

Denote by $\mathrm{E}^*_{\mathrm{tot}}(t,\omega)$ and $\mathrm{T}^*_{\mathrm{tot}}(t,\omega)$ the total number of molecules of E* and T* in D_{eff} at time t, for the random event ω of Rh*,

$$\mathrm{E}^*_{\mathrm{tot}}(t,\omega) = \int_{\mathrm{D_{eff}}}[\mathrm{E}^*](x,y,t;\omega)dxdy,$$
$$T^*_{\mathrm{tot}}(t,\omega) = \int_{\mathrm{D_{eff}}}[\mathrm{T}^*](x,y,t;\omega)dxdy.$$

Integrating the equations if Eq. 1 in $dxdy$ over D_{eff}, and taking into account the no-flux boundary conditions in Eq. 2, gives

$$\begin{aligned}
&\frac{d}{dt}\mathrm{T}^*_{\mathrm{tot}}(t,\omega) = \mathrm{Rh}^*(t,\omega) - N(t,\omega) \quad \mathrm{T}^*_{\mathrm{tot}}(0,\omega) = 0 \\
&\frac{d}{dt}\mathrm{E}^*_{\mathrm{tot}}(t,\omega) = N(t,\omega) - k_{\mathrm{E}}\mathrm{E}^*_{\mathrm{tot}}(t,\omega) \quad \mathrm{E}^*_{\mathrm{tot}}(0,\omega) = 0, \qquad (14)
\end{aligned}$$

where $N(\cdot,\omega)$ is the nonlinear random term

$$N(t,\omega) = k_{\mathrm{T^*E}}\int_{\mathrm{D_{eff}}}[\mathrm{E}][\mathrm{T}^*](x,y,t,\omega)dxdy.$$

Let $\{X,\Omega,d\omega\}$ denote the probability space of the random events of Rh*, and let $\langle\cdot\rangle$ denote the expected values of a random variable over $\{X,\Omega,d\omega\}$. Thus,

$$\langle\mathrm{E}^*_{\mathrm{tot}}\rangle(t) = \int_{\mathrm{X}}\mathrm{E}^*_{\mathrm{tot}}(t,\omega)d\omega, \quad \langle\mathrm{Rh}^*\rangle(t) = \int_{\mathrm{X}}\mathrm{Rh}^*(t,\omega)d\omega,$$

and let $\langle T^*_{tot}\rangle$ and $\langle N\rangle$ be defined analogously. Then, in terms of expected values,

$$\frac{d}{dt}\langle T^*_{tot}\rangle = \langle Rh^*\rangle - \langle N\rangle \quad \langle T^*_{tot}\rangle(0) = 0$$

$$\frac{d}{dt}\langle E^*_{tot}\rangle = \langle N\rangle - k_E\langle E^*_{tot}\rangle \quad \langle E^*_{tot}\rangle(0) = 0.$$

It is assumed that, regardless of the random events of Rh*, the system returns to its initial steady state after a time, which, without loss of generality, may assume to be asymptotic to infinity. Therefore,

$$T^*_{tot}(0,\omega) = E^*_{tot}(0,\omega) = T^*_{tot}(t_\infty,\omega) = E^*_{tot}(t_\infty,\omega) = 0.$$

Denote by $E^{**}(\omega)$ and $T^{**}(\omega)$ the random, total number of molecules of E* and T* produced over the entire time-duration of the process, so that

$$E^{**}(\omega) = \int_0^\infty E^*_{tot}(t,\omega)dt, \quad T^{**}(\omega) = \int_0^\infty T^*_{tot}(t,\omega)dt.$$

Integrating Eq. 14 in dt over $[0, \infty)$ and eliminating the terms involving the nonlinear term $N(\cdot, \omega)$, gives

$$k_E E^{**} = \sum_{j=1}^{n} \nu_j \int_0^\infty \chi_{(t_{j-1},t_j]}(t)dt = \sum_{j=1}^{n} \nu_j \bar{\tau}_j(\omega),$$

where $\bar{\tau}_j$ is the random duration of the j^{th} state. From this,

$$k_E\langle E^{**}\rangle = \sum_{j=1}^{n} \nu_j \int_X \bar{\tau}_j(\omega)d\omega = \sum_{j=1}^{n} \nu_j\tau_j.$$

Using the independence of random durations $\bar{\tau}_j$, and their exponential distribution, with mean τ_j, one computes also the variance of E**,

$$\begin{aligned} k_E^2\sigma^2_{E^{**}} &= \int_X \Big|\sum_{j=1}^{n} \nu_j\big[\bar{\tau}_j(\omega) - \tau_j\big]\Big|^2 d\omega \\ &= \sum_{j=1}^{n} \nu_j^2\left(\int_X \bar{\tau}_j^2(\omega)d\omega - \tau_j^2\right) \\ &= \sum_{j=1}^{n} \nu_j^2\left(\int_0^\infty \tau^2\frac{1}{\tau_j}e^{(-\tau/\tau_j)}d\tau - \tau_j^2\right) = \sum_{j=1}^{n} \nu_j^2\tau_j^2. \end{aligned}$$

Therefore, the CV of E** is given by

$$CV(E^{**}) = \frac{\sqrt{\sum_{j=1}^{n}(\nu_j\tau_j)^2}}{\sum_{j=1}^{n}\nu_j\tau_j}. \tag{15}$$

More on statistics and biochemistry

Since the sequences $\{\nu_j\}$ and $\{\tau_j\}$ reflect the underlying biochemistry, the theoretical formula (Eq. 15) can be used to constrain some combinations of these parameters. For example:

1. Decreasing catalytic constants $k_j = \nu_{RE}/b^{j-1}$ for some $b > 1$, and increasing time steps $\tau_j = b^{j-(\ell+1)}\tau_{Rh^*}$, for some positive integer ℓ. Therefore, $k_j\tau_j = \nu_{RE}\tau_{Rh^*}/b^\ell$ for all j and $CV(E^{**}) = 1/\sqrt{n}$.
2. Increasing catalytic constants $k_j = \nu_{RE}$ and decreasing time steps $\tau_j = \tau_{Rh^*}/b^j$. Therefore, $k_j\tau_j = \nu_{RE}\tau_{Rh^*}/b^j$ for all j and Eq. 15 implies that $CV(E^{**}) > \sqrt{(b-1)/(b+1)}$ as $n \to \infty$.
3. Decreasing catalytic constants $k_j = \nu_{RE}/b^{j-1}$ and decreasing time steps $\tau_j = \tau_{Rh^*}/b^j$. Therefore, $k_j\tau_j = \nu_{RE}\tau_{Rh^*}/b^{2j-1}$ for all j and Eq. 15 implies that $CV(E^{**}) > 1/\sqrt{b^2+1}$ as $n \to \infty$.

Therefore, $CV(E^{**}) \to 0$ as $n \to \infty$, only in the Case 1. In the remaining cases, $CV(E^{**})$ never goes to zero as $n \to \infty$.

By the experimental data of the literature (6–8), the CV of the current suppression goes to zero as $n \to \infty$ and this is possible only if $CV(E^{**}) \to 0$ as $n \to \infty$ (although not necessarily as $1/\sqrt{n}$). This rules out the corresponding biochemical mechanisms. Returning to Case 1, it should be pointed out that this is only a sufficient condition for $CV(E^{**}) \to 0$ as $n \to \infty$ and does not necessarily point to a precise biochemistry. Choices of this kind appear in the literature (45,46), although we are not aware of a biochemical basis for them. In any case, Eq. 15 affords a spectrum of possible tests. For example, if one of them decreases harmonically, say $\nu_j = \nu_{RE}/j$, whereas the other remains constant, then the corresponding $CV(E^{**})$ goes to zero as $n \to \infty$ like $1/\ln n$.

We thank Dr. Fred Rieke for mouse electrophysiological data.

This work was supported by National Institutes of Health grant No. 1-RO1-GM-068953-01, and conducted in part using the resources of the Advanced Computing Center for Research and Education at Vanderbilt University, Nashville, Tennessee.

REFERENCES

1. Aho, A. C., K. Donner, C. Hyden, L. O. Larsen, and T. Reuter. 1988. Low retinal noise in animals with low body temperature allows high visual sensitivity. *Nature*. 334:348–350.
2. Hecht, S., S. Shlaer, and M. Pierenne. 1942. Energy, quanta and vision. *J. Gen. Physiol*. 25:819–840.
3. Baylor, D. A., T. D. Lamb, and K. W. Yau. 1979. The membrane current of single rod outer segments. *J. Physiol*. 288:589–611.
4. Baylor, D. A., T. D. Lamb, and K. W. Yau. 1979. Responses of retinal rods to single photons. *J. Physiol*. 288:613–634.
5. Felber, S., H. P. Breuer, F. Petruccione, J. Honerkamp, and K. P. Hofmann. 1996. Stochastic simulation of the transducin GTPase cycle. *Biophys. J*. 71:3051–3063.
6. Rieke, F., and D. A. Baylor. 1998. Origin of reproducibility in the responses of retinal rods to single photons. *Biophys. J*. 75:1836–1857.
7. Rieke, F., and D. A. Baylor. 1998. Single photon detection by rod cells of the retina. *Rev. Mod. Phys*. 70:1027–1036.
8. Whitlock, G. G., and T. D. Lamb. 1999. Variability in the timecourse of single photon responses from toad rods: termination of rhodopsin's activity. *Neuron*. 23:337–351.
9. Ramanathan, S., P. B. Detwiler, A. M. Sengupta, and B. I. Shraiman. 2005. G-protein-coupled enzyme cascades have intrinsic properties that improve signal localization and fidelity. *Biophys. J*. 88:3063–3071.
10. Pugh, E. N. 1999. Variability of single photon responses: a cut in the Gordian knot of rod phototransduction? *Neuron*. 23:205–208.
11. Liebman, P. A., and E. N. Pugh. 1979. The control of phosphodiesterase in rod disk membranes: kinetics, possible mechanisms, and significance for vision. *Vision Res*. 19:375–380.
12. Liebman, P. A., K. R. Parker, and E. A. Dratz. 1987. The molecular mechanism of visual excitation and its relation to the structure and composition of the rod outer segment. *Annu. Rev. Physiol*. 49:765–791.
13. Andreucci, D., P. Bisegna, G. Caruso, H. E. Hamm, and E. DiBenedetto. 2003. Mathematical model of the spatiotemporal dynamics of second messengers in visual transduction. *Biophys. J*. 85:1358–1376.
14. Caruso, G., H. Khanal, V. Alexiades, F. Rieke, H. E. Hamm, and E. DiBenedetto. 2005. Mathematical and computational modeling of spatiotemporal signaling in rod phototransduction. *IEE Proc. Sys. Biol*. 152:119–137.
15. Caruso, G., P. Bisegna, L. Shen, D. Andreucci, H. E. Hamm, and E. DiBenedetto. 2006. Modeling the role of incisures in vertebrate phototransduction. *Biophys. J*. 91:1192–1212.
16. Pugh, E. N., Jr., and T. D. Lamb. 2000. Phototransduction in vertebrate rods and cones: molecular mechanisms of amplification, recovery and light adaptation. *In* Handbook of Biological Physics, Vol. 3. Elsevier Science, St. Louis, MO.

17. Pugh, Jr., E. N., and T. Lamb. 1993. Amplification and kinetics of the activation steps in phototransduction. *Biochim. Biophys. Acta.* 1141:111–149.

18. Vishnivetskiy, S. A., D. Raman, J. Wei, M. J. Kennedy, J. B. Hurley, and V. V. Gurevich. 2007. Regulation of arrestin binding by rhodopsin phosphorylation level. *J. Biol. Chem.* 282:32075–32083.

19. Ohguro, H., J. P. Van Hooser, A. H. Milam, and K. Palczewski. 1995. Rhodopsin phosphorylation and dephosphorylation in vivo. *J. Biol. Chem.* 270:14259–14262.

20. Wilden, U., S. W. Hall, and H. Kuhn. 1986. Phosphodiesterase activation by photoexcited rhodopsin is quenched when rhodopsin is phosphorylated and binds the intrinsic 48-kDa protein of rod outer segments. *Proc. Natl. Acad. Sci. USA.* 83:1174–1178.

21. Chen, J., C. L. Makino, N. S. Peachey, D. A. Baylor, and M. I. Simon. 1995. Mechanisms of rhodopsin inactivation in vivo as revealed by a COOH-terminal truncation mutant. *Science.* 267:374–377.

22. Xu, J., R. L. Dodd, C. L. Makino, M. I. Simon, D. A. Baylor, and J. Chen. 1997. Prolonged photoresponses in transgenic mouse rods lacking arrestin. *Nature.* 389:505–509.

23. Krispel, C. M., D. Chen, N. Melling, Y. J. Chen, K. A. Martemyanov, N. Quillinan, V. Y. Arshavsky, T. G. Wensel, C. K. Chen, and M. E. Burns. 2006. RGS expression rate-limits recovery of rod photoresponses. *Neuron.* 51:409–416.

24. Baylor, D. A., G. Matthews, and K. W. Yau. 1980. Two components of electrical dark noise in toad retinal rod outer segments. *J. Physiol.* 309:591–621.

25. Rieke, F., and D. A. Baylor. 1996. Molecular origin of continuous dark noise in rod photoreceptors. *Biophys. J.* 71:2553–2572.

26. Baylor, D. A., B. J. Nunn, and J. L. Schnapf. 1984. The photocurrent, noise and spectral sensitivity of rods of the monkey *Macaca fascicularis*. *J. Physiol.* 357:575–607.

27. Sakitt, B. 1972. Counting every quantum. *J. Physiol.* 223:131–150.

28. Field, G. D., and F. Rieke. 2002. Mechanisms regulating variability of the single photon responses of mammalian rod photoreceptors. *Neuron.* 35:733–747.

29. Andreucci, D., P. Bisegna, and E. DiBenedetto. 2003. Homogenization and concentrated capacity for the heat equation with nonlinear variational data in reticular almost disconnected structures and applications to visual transduction. *Ann. Mat. Pure Appl.* 182:375–407.

30. Andreucci, D., P. Bisegna, and E. DiBenedetto. 2006. Homogenization and concentration of capacity in phototransduction in vertebrate photoreception. *Appl. Anal.* 85:303–331 (Special Issue in honor of C. Pucci.).

31. Makino, C. L., R. L. Dodd, J. Chen, M. E. Burns, A. Roca, M. I. Simon, and D. A. Baylor. 2004. Recoverin regulates light-dependent phosphodiesterase activity in retinal rods. *J. Gen. Physiol.* 123:729–741.

32. Wilden, U. 1995. Duration and amplitude of the light-induced cGMP hydrolysis in vertebrate photoreceptors are regulated by multiple phosphorylation of rhodopsin and by arrestin binding. *Biochemistry.* 34:1446–1454.

33. Gibson, S. K., J. H. Parkes, and P. A. Liebman. 2000. Phosphorylation modulates the affinity of light-activated rhodopsin for G protein and arrestin. *Biochemistry.* 39:5738–5749.

34. Senin, I. I., K. W. Koch, M. Akhtar, and P. P. Philippov. 2002. Ca^{2+}-dependent control of rhodopsin phosphorylation: recoverin and rhodopsin kinase. *Adv. Exp. Med. Biol.* 514:69–99.

35. Pullen, N., N. G. Brown, R. P. Sharma, and M. Akhtar. 1993. Cooperativity during multiple phosphorylations catalyzed by rhodopsin kinase: supporting evidence using synthetic phosphopeptides. *Biochemistry.* 32:3958–3964.

36. Brannock, M. T., K. Weng, and P. R. Robinson. 1999. Rhodopsin's carboxyl-terminal threonines are required for wild-type arrestin-mediated quench of transducin activation in vitro. *Biochemistry.* 38:3770–3777.

37. Aton, B. R., B. J. Litman, and M. L. Jackson. 1984. Isolation and identification of the phosphorylated species of rhodopsin. *Biochemistry.* 23:1737–1741.

38. Wilden, U., and H. Kuhn. 1982. Light-dependent phosphorylation of rhodopsin: number of phosphorylation sites. *Biochemistry.* 21:3014–3022.

39. Pulvermuller, A., K. Palczewski, and K. P. Hofmann. 1993. Interaction between photoactivated rhodopsin and its kinase: stability and kinetics of complex formation. *Biochemistry.* 32:14082–14088.

40. Mendez, A., M. E. Burns, A. Roca, J. Lem, L. W. Wu, M. I. Simon, D. A. Baylor, and J. Chen. 2000. Rapid and reproducible deactivation of rhodopsin requires multiple phosphorylation sites. *Neuron.* 28:153–164.

41. Nair, K. S., S. M. Hanson, A. Mendez, E. V. Gurevich, M. J. Kennedy, V. I. Shestopalov, S. A. Vishnivetskiy, J. Chen, J. B. Hurley, V. V. Gurevich, and V. Z. Slepak. 2005. Light-dependent redistribution of arrestin in vertebrate rods is an energy-independent process governed by protein-protein interactions. *Neuron.* 46:555–567.

42. Hanson, S. M., E. V. Gurevich, S. A. Vishnivetskiy, M. R. Ahmed, X. Song, and V. V. Gurevich. 2007. Each rhodopsin molecule binds its own arrestin. *Proc. Natl. Acad. Sci. USA.* 104:3125–3128.

43. Strissel, K. J., M. Sokolov, L. H. Trieu, and V. Y. Arshavsky. 2006. Arrestin translocation is induced at a critical threshold of visual signaling and is superstoichiometric to bleached rhodopsin. *J. Neurosci.* 26:1146–1153.

44. Hanson, S. M., N. Van-Eps, D. J. Francis, C. Altenbach, S. A. Vishnivetskiy, V. Y. Arshavsky, C. S. Klug, W. L. Hubbell, and V. V. Gurevich. 2007. Structure and function of the visual arrestin oligomer. *EMBO J.* 26:1726–1736.

45. Doan, T., A. Mendez, P. B. Detwiler, J. Chen, and F. Rieke. 2006. Multiple phosphorylation sites confer reproducibility of the rod's single-photon responses. *Science.* 313:530–533.

46. Hamer, R. D., S. C. Nicholas, D. Tranchina, P. A. Liebman, and T. D. Lamb. 2003. Multiple steps of phosphorylation of activated rhodopsin can account for the reproducibility of vertebrate rod single-photon responses. *J. Gen. Physiol.* 122:419–444.

47. Chen, C. K., M. E. Burns, W. He, T. G. Wensel, D. A. Baylor, and M. I. Simon. 2000. Slowed recovery of rod photoresponse in mice lacking the GTPase accelerating protein RGS9–1. *Nature.* 403:557–560.

48. Chen, C. K., M. E. Burns, M. Spencer, G. A. Niemi, J. Chen, J. B. Hurley, D. A. Baylor, and M. I. Simon. 1999. Abnormal photoresponses and light-induced apoptosis in rods lacking rhodopsin kinase. *Proc. Natl. Acad. Sci. USA.* 96:3718–3722.

49. Nikonov, S., T. D. Lamb, and E. N. Pugh, Jr. 2000. The role of steady phosphodiesterase activity in the kinetics and sensitivity of the light-adapted salamander rod photoresponse. *J. Gen. Physiol.* 116:795–824.

50. Lyubarsky, A. L., S. Nikonov, and E. N. Pugh, Jr. 1996. The kinetics of inactivation of the rod phototransduction cascade with constant Ca_i^{2+}. *J. Gen. Physiol.* 107:19–34.

51. Lyubarsky, A. L., and E. N. Pugh, Jr. 1996. Recovery phase of the murine rod photoresponse reconstructed from electroretinographic recordings. *J. Neurosci.* 16:563–571.

52. Hood, D. C., and D. G. Birch. 1995. Phototransduction in human cones measured using the α-wave of the ERG. *Vision Res.* 35:2801–2810.

53. Gray-Keller, M., W. Denk, B. Shraiman, and P. B. Detwiler. 1999. Longitudinal spread of second messenger signals in isolated rod outer segments of lizards. *J. Physiol.* 519:679–692.

54. Leskov, I. B., V. A. Klenchin, J. W. Handy, G. G. Whitlock, V. I. Govardovskii, M. D. Bownds, T. D. Lamb, E. N. Pugh, Jr., and V. Y. Arshavsky. 2000. The gain of rod phototransduction: reconciliation of biochemical and electrophysiological measurements. *Neuron.* 27:525–537.

55. Olson, A., and E. N. Pugh, Jr. 1993. Diffusion coefficient of cyclic GMP in salamander rod outer segments estimated with two fluorescent probes. *Biophys. J.* 65:1335–1352.

56. Cohen, A. I. 1960. The ultrastructure of the rods of the mouse retina. *Am. J. Anat.* 107:23–48.

57. Carter-Dawson, L. D., and M. M. Lavail. 1979. Rods and cones in the mouse retina. *J. Comp. Neurol.* 188:245–262.

58. Rieke, F., and D. A. Baylor. 2000. Origin and functional impact of dark noise in retinal cones. *Neuron.* 26:181–186.

59. Holcman, D., and J. I. Korenbrot. 2004. Longitudinal diffusion in retinal rod and cone outer segment cytoplasm: the consequence of cell structure. *Biophys. J.* 86:2566–2582.
60. Chang, G. Q., Y. Hao, and F. Wong. 1993. Apoptosis: final common pathway of photoreceptor death in rd, rds, and rhodopsin mutant mice. *Neuron.* 11:595–605.
61. Nikonov, S., N. Engheta, and E. N. Pugh, Jr. 1998. Kinetics of recovery of the dark-adapted salamander rod photoresponse. *J. Gen. Physiol.* 111:7–37.
62. Lamb, T. D., and E. N. Pugh, Jr. 1992. A quantitative account of the activation steps involved in phototransduction in amphibian photoreceptors. *J. Physiol.* 449:719–758.
63. Koutalos, Y., K. Nakatani, and K. W. Yau. 1995. Cyclic GMP diffusion coefficients in rod photoreceptor outer segments. *Biophys. J.* 68: 373–382.
64. Nakatani, K., C. Chen, and Y. Koutalos. 2002. Calcium diffusion coefficient in rod photoreceptor outer segments. *Biophys. J.* 82:728–739.
65. Eckmiller, M. S. 2000. Microtubules in a rod-specific cytoskeleton associated with outer segment incisures. *Vis. Neurosci.* 17:711–722.
66. Tsukamoto, Y. 1987. The number, depth and elongation of disk incisures in the retinal rod of *Rana catesbiana*. *Exp. Eye Res.* 45:105–116.
67. Papermaster, D. S., P. Reilly, and B. G. Schneider. 1982. Cone lamellae and red and green rod outer segment disks contain a large intrinsic membrane protein on their margins: an ultrastructural immunocytochemical study of frog retinas. *Vision Res.* 22:1417–1428.
68. Liang, Y., D. Fotiadis, S. Filipek, D. A. Saperstein, K. Palczewski, and A. Engel. 2003. Organization of the G protein-coupled receptors rhodopsin and opsin in native membranes. *J. Biol. Chem.* 278:21655–21662.
69. Roof, D., M. Adamian, D. Jacobs, and A. Hayes. 1991. Cytoskeletal specializations at the rod photoreceptor distal tip. *J. Comp. Neurol.* 305:289–303.
70. Calvert, P. D., V. I. Govardovskii, N. Krasnoperova, R. E. Anderson, J. Lem, and C. L. Makino. 2001. Membrane protein diffusion sets the speed of rod phototransduction. *Nature.* 411:90–94.
71. Tsang, S. H., M. E. Burns, P. D. Calvert, P. Gouras, D. A. Baylor, S. P. Goff, and V. Y. Arshavsky. 1998. Role for the target enzyme in deactivation of photoreceptor G protein in vivo. *Science.* 282:117–121.
72. Burns, M. E., A. Mendez, J. Chen, and D. A. Baylor. 2002. Dynamics of cyclic GMP synthesis in retinal rods. *Neuron.* 36:81–91.
73. Pugh, E. N., Jr., T. Duda, A. Sitaramayya, and R. K. Sharma. 1997. Photoreceptor guanylate cyclases: a review. *Biosci. Rep.* 17:429–473.
74. Pugh, E. N., Jr., and T. Lamb. 1990. Cyclic GMP and calcium: the internal messengers of excitation and adaptation in vertebrate photoreceptors. *Vision Res.* 30:1923–1948.
75. Detwiler, P. B., S. Ramanathan, A. Sengupta, and B. I. Shraiman. 2000. Engineering aspects of enzymatic signal transduction: photoreceptors in the retina. *Biophys. J.* 79:2801–2817.
76. Gray-Keller, M. P., and P. B. Detwiler. 1994. The calcium feedback signal in the phototransduction cascade of vertebrate rods. *Neuron.* 13:849–861.
77. Korenbrot, J. I., and D. Miller. 1989. Cytoplasmic free calcium concentration in dark-adapted retinal rod outer segments. *Vision Res.* 29:939–948.
78. Lagnado, L., L. Cervetto, and P. A. McNaughton. 1992. Calcium homeostasis in the outer segments of retinal rods from the tiger salamander. *J. Physiol.* 455:111–142.
79. McCarthy, S. T., J. P. Younger, and W. G. Owen. 1994. Free calcium concentrations in bullfrog rods determined in the presence of multiple forms of Fura-2. *Biophys. J.* 67:2076–2089.
80. Ratto, G. M., R. Payne, W. G. Owen, and R. Y. Tsien. 1988. The concentration of cytosolic free calcium in vertebrate rod outer segments measured with Fura-2. *J. Neurosci.* 8:3240–3246.
81. Sampath, A. P., H. R. Matthews, M. C. Cornwall, and G. L. Fain. 1998. Bleached pigment produces a maintained decrease in outer segment Ca^{2+} in salamander rods. *J. Gen. Physiol.* 111:53–64.
82. Woodruff, M. L., A. P. Sampath, H. R. Matthews, N. V. Krasnoperova, J. Lem, and G. L. Fain. 2002. Measurement of cytoplasmic calcium concentration in the rods of wild-type and transducin knock-out mice. *J. Physiol.* 542:843–854.
83. Fotiadis, D., Y. Liang, S. Filipek, D. A. Saperstein, A. Engel, and K. Palczewski. 2003. Rhodopsin dimers in native disk membranes. *Nature.* 421:127–128.
84. Reilander, H., A. Achilles, U. Friedel, G. Maul, F. Lottspeich, and N. J. Cook. 1992. Primary structure and functional expression of the Na/Ca,K-exchanger from bovine rod photoreceptors. *EMBO J.* 11:1689–1695.
85. Schnetkamp, P. P. 1990. Cation selectivity of and cation binding to the cGMP-dependent channel in bovine rod outer segment membranes. *J. Gen. Physiol.* 96:517–534.
86. Liang, Y., D. Fotiadis, T. Maeda, A. Maeda, A. Modzelewska, S. Filipek, D. A. Saperstein, A. Engel, and K. Palczewski. 2004. Rhodopsin signaling and organization in heterozygote rhodopsin knockout mice. *J. Biol. Chem.* 279:48189–48196.
87. Lyubarsky, A. L., L. L. Daniele, and E. N. Pugh, Jr. 2004. From candelas to photoisomerizations in the mouse eye by rhodopsin bleaching in situ and the light-rearing dependence of the major components of the mouse ERG. *Vision Res.* 44:3235–3251.
88. Fan, J., M. L. Woodruff, M. C. Cilluffo, R. K. Crouch, and G. L. Fain. 2005. Opsin activation of transduction in the rods of dark-reared Rpe65 knockout mice. *J. Physiol.* 568:83–95.
89. Krispel, C. M., C. K. Chen, M. I. Simon, and M. E. Burns. 2003. Novel form of adaptation in mouse retinal rods speeds recovery of phototransduction. *J. Gen. Physiol.* 122:703–712.
90. Krispel, C. M., C. K. Chen, M. I. Simon, and M. E. Burns. 2003. Prolonged photoresponses and defective adaptation in rods of $G\beta5-/-$ mice. *J. Neurosci.* 23:6965–6971.
91. Mendez, A., M. E. Burns, I. Sokal, A. M. Dizhoor, W. Baehr, K. Palczewski, D. A. Baylor, and J. Chen. 2001. Role of guanylate cyclase-activating proteins (GCAPs) in setting the flash sensitivity of rod photoreceptors. *Proc. Natl. Acad. Sci. USA.* 98:9948–9953.
92. Mendez, A., and J. Chen. 2002. Mouse models to study GCAP functions in intact photoreceptors. *Adv. Exp. Med. Biol.* 514:361–388.
93. Wang, Z., X. H. Wen, Z. Ablonczy, R. K. Crouch, C. L. Makino, and J. Lem. 2005.Enhanced shutoff of phototransduction in transgenic mice expressing palmitoylation-deficient rhodopsin. *J. Biol. Chem.* 280:24293–24300.
94. Woodruff, M. L., J. Lem, and G. L. Fain. 2004. Early receptor current of wild-type and transducin knockout mice: photosensitivity and light-induced Ca^{2+} release. *J. Physiol.* 557:821–828.
95. Schnetkamp, P. P. 1989. Na-Ca or Na-Ca-K exchange in rod photoreceptors. *Prog. Biophys. Mol. Biol.* 54:1–29.
96. Schnetkamp, P. P. 1991. Optical measurements of Na-Ca-K exchange currents in intact outer segments isolated from bovine retinal rods. *J. Gen. Physiol.* 98:555–573.
97. Schnetkamp, P. P., R. T. Szerencsei, and D. K. Basu. 1991. Unidirectional Na^+, Ca^{2+}, and K^+ fluxes through the bovine rod outer segment Na-Ca-K exchanger. *J. Biol. Chem.* 266:198–206.
98. Qin, N., and W. Baehr. 1994. Expression and mutagenesis of mouse rod photoreceptor cGMP phosphodiesterase. *J. Biol. Chem.* 269: 3265–3271.
99. Kennedy, M. J., M. E. Sowa, T. G. Wensel, and J. B. Hurley. 2003. Acceleration of key reactions as a strategy to elucidate the rate-limiting chemistry underlying phototransduction inactivation. *Invest. Ophthalmol. Vis. Sci.* 44:1016–1022.
100. Sitaramayya, A., J. Harkness, J. H. Parkes, C. Gonzalez-Oliva, and P. A. Liebman. 1986. Kinetic studies suggest that light-activated cyclic GMP phosphodiesterase is a complex with G-protein subunits. *Biochemistry.* 25:651–656.
101. Lem, J., N. V. Krasnoperova, P. D. Calvert, B. Kosaras, D. A. Cameron, M. Nicolo, C. L. Makino, and R. L. Sidman. 1999. Morphological, physiological, and biochemical changes in rhodopsin knockout mice. *Proc. Natl. Acad. Sci. USA.* 96:736–741.